Student thesis series INES nr 537

Estimating active layer thickness at the high Arctic study site Zackenberg from remotely sensed ground subsidence

Lotte Wendt

2021
Department of
Physical Geography and Ecosystem Science
Lund University
Sölvegatan 12
S-223 62 Lund
Sweden

Lotte Wendt (2021).

Estimating active layer thickness at the high Arctic study site Zackenberg from remotely sensed ground subsidence (English).

Uppskattning av det aktiva lagrets tjocklek från fjärranalyserad marksättning vid det högarktiska studieområdet Zackenberg (Swedish).

Bachelor degree thesis, 15 credits in Physical Geography and Ecosystem Analysis
Department of Physical Geography and Ecosystem Science, Lund University

Level: Bachelor of Science (BSc)

Course duration: *November* 2020 until *January* 2021

Disclaimer

This document describes work undertaken as part of a program of study at the University of Lund. All views and opinions expressed herein remain the sole responsibility of the author, and do not necessarily represent those of the institute.

Estimating active layer thickness at the high Arctic study site Zackenberg from remotely sensed ground subsidence

---

Lotte Wendt

Bachelor thesis, 15 credits, in Physical Geography and Ecosystem Analysis

Supervisor:

Marko Scholze
Department of Physical Geography and Ecosystem Science,
Lund University

Exam committee:

Lars Harrie

Thomas Pugh

Department of Physical Geography and Ecosystem Science,
Lund University

Acknowledgements

I would like to thank my supervisor Marko Scholze for his encouragement to approach a method I was highly interested in, even though the outcome was unknown at the start of my thesis work. The weekly meetings and your feedback to my thesis progress were very helpful. Thank you as well to my examiners Lars Harrie and Thomas Pugh as well as to my critic Hugo Bergman for valuable input. Thanks to GeoBasis Zackenberg, especially Daniel A. Rudd, for providing data and welcoming me at Zackenberg research station as a field assistant. I would also like to thank Andreas Braun from the University Tübingen for help with questions about the SNAP processing. I am very grateful to have studied with so wonderful classmates and wish all of you the best. And lastly, thanks to my family and partner, for always having my back.

Abstract

The active layer thickness (ALT) is an indicator of permafrost thaw, which potentially leads to the release of large amounts of greenhouse gases under global warming, and thus could further amplify climate change. The thaw depth of the active layer also governs seasonal surface deformation, caused by the volume change between ice to water, which poses risks for slope stability and infrastructure foundations. Currently, the monitoring of the ALT is accomplished through modelling and field measurements. This thesis aims at testing a recently introduced remote sensing method for ALT monitoring by comparing the estimated ALT to ALT field measurements and environmental parameters. The method is based on remotely sensed seasonal ground subsidence, derived through the differential interferometric synthetic aperture radar technique (DInSAR). By estimating the ice content in the soil, the ground subsidence can be related to ALT development, which was used to determine the ALT throughout the thawing season 2017 at Zackenberg valley, Greenland. The ice content was derived by combining saturation fraction with porosity. The saturation fraction was determined based on a linear regression between the normalized soil moisture index and soil moisture measurements. The porosity was obtained through organic matter field measurements and a mineral soil database. The resulting ALT estimate was statistically similar to the ALT field measurements, both considering ALT maximum (p-value = 0.55) and temporal development (agreement to ideal fit: p-value = 0.33). The ALT distribution is plausible considering environmental factors (aspect, topography, vegetation). Yet, the method was found to perform best in water-saturated areas and showed more variable results in drier areas. For future applications it is recommended to incorporate modelling of the subsurface ice content, as the ALT result in drier soils is especially dependent on a correct estimate of the ice content. If this is accomplished, and if the subsidence retrieval considers 3D-ground displacement, the tested method is promising for the ALT monitoring at high spatial resolution during the snow-free season.

Keywords: *Active layer thickness, DInSAR, subsidence, Permafrost, Zackenberg, CALM*

Popular Summary

Permafrost covers 14 % of Earth's land surface and is defined as soil which has been continuously frozen for at least two years. Due to global warming, permafrost soils experience thawing. This has to be monitored because the thawing could release greenhouse gases from previously frozen organic soil as well as affect ground stability and thereby infrastructure. Permafrost thaw is indicated by a deepening of the upper soil layer, which thaws during the summer. This so-called active layer and its thickness (ALT) can be monitored through modelling or field measurements. Yet, these methods are limited by data resolution and available labour.

This thesis aimed at testing a new method presented by Liu et al. (2012) for ALT estimation. For this, the method was applied across Zackenberg valley in NE Greenland to estimate the ALT during the thaw season of 2017. Then, the result was evaluated through comparison with field measurements and relationships to environmental factors.

The tested method is based on ground subsidence estimated through radar satellite imagery. As ground subsidence during the thawing season is a result of the volume change of water from ice to liquid in the soil, the ALT can be estimated if subsidence and ice content are known. In this study, the relationship between a satellite-based soil moisture index and soil moisture measurements was used to map the saturation across the study area. The porosity of the soil was estimated from field measurements and a soil database. By combining ground subsidence with ice content based on saturation and porosity, the ALT development and maximum ALT could be estimated.

Both the resulting maximum estimated ALT and the temporal development were statistically similar to the field measurements. The estimated ALT was deepest on southern slopes, which aligns with more available energy for thawing due to more incoming solar radiation compared to other slope directions. Shallower ALT was found in wetlands, which thaw slower due to insulating peat layers and high ice content. The error in ALT estimate was largest in drier areas, shown by larger differences to field measurements. This was also supported by larger discrepancies of the ALT estimate in dry vegetation types to the expected values from literature. The error can be related to increased sensitivity of the method to accurate ice content estimates in drier soils.

The method is promising for intermediate scale ALT mapping and can be applied in water-saturated areas. For other areas, it is recommended to refine the method by including soil saturation modelling and to evaluate the estimate with more extensive field measurements.

Table of Contents

1 Introduction 1

1.1 Study aim 2

1.2 Hypothesis 2

2 Background 3

2.1 Active layer dynamics 3

2.2 Ground subsidence and the DInSAR method 5

2.3 Previous studies 7

3 Methodology 8

3.1 Study site 8

3.2 Data and processing environment 9

3.3 Active layer thickness estimation 9

3.3.1 DInSAR subsidence 10

3.3.2 Estimation of porosity 11

3.3.3 Estimation of saturation fraction 11

3.3.4 Active layer thickness calculation 12

3.4 Field measurements of ALT 13

3.4.1 Processing 13

3.4.2 Resulting field measurement data 14

3.5 Evaluation of estimated active layer thickness 14

4 Results 16

4.1 Derived soil moisture and porosity 16

4.2 Evaluation of subsidence 18

4.3 Estimated active layer thickness 18

4.4 Accuracy evaluation with field measurements 19

4.5 Accuracy evaluation with environmental parameters 21

5 Discussion 24

5.1 Ability of method to estimate ALT 24

5.2 Sources of error in study 26

5.3 Overall method evaluation and comparison 27

5.3.1 Limitations of method 27

5.3.2 Comparison to other methods 29

6 Conclusion 30

7 References 31

8 Appendix 36

1 Introduction

Permafrost is defined as ground which has been continuously frozen for at least two years (Muller 1947; Permafrost Subcommittee 1988) and can thus be found both at high latitudes and in high elevations. Regions underlain by permafrost cover 14% of the global landmass and 24 % of the landmass in the northern hemisphere (Zhang et al. 2008; Gruber 2012).

Permafrost regions are expected to store 1,330–1,580 Pg carbon in the upper 0 – 3 m of the soil column (Hugelius et al. 2014). This accounts for half of the global soil organic carbon and equals roughly two times the amount of carbon currently in the atmosphere (Gruber 2012; Hugelius et al. 2014). The stored carbon stock is not actively cycling, because decomposition is strongly inhibited by low temperatures in the frozen permafrost soils (Walz et al. 2017). New carbon stocks from permafrost soils become available to microbial decomposition when the permafrost thaws and thus, the active layer deepens. The active layer (AL) is defined as seasonally unfrozen upper soil layer (Permafrost Subcommittee 1988). The greenhouse gas emissions resulting from the microbial breakdown of the through thawing released carbon can further amplify climate change (Schuur et al. 2015).

Besides the release of stored carbon, changes in active layer thickness (ALT) also affect local hydrology and ground stability (Nelson et al. 2002; Hong 2014). Due to the seasonal thawing of ground ice in the AL, subsidence is caused, which varies in magnitude depending on the ground ice contents in the soil and the thaw depth. The surface deformation endangers the stability of house foundations as well as other engineering structures (Hong 2014). Further, the thawing reduces the strength of ice-rich sediments on slopes, which poses the risk of slope destabilization and could increase slope failure and landslides (Akerman 2005; Harris 2005; Niu et al. 2014). As the permafrost acts as drainage barrier, it also has a large influence on the local hydrology and increases in ALT affect water fluxes including soil moisture and ground water storage (Walvoord and Kurylyk 2016).

Due to these impacts of permafrost thaw, it is of large importance to monitor the state of the active layer, for which increases in thickness in response to global warming have been observed across the entire permafrost region (Biskaborn et al. 2019).

The main field methods for ALT monitoring are manual probing and interpolation of temperature measurements along a depth gradient. These observations are, however, limited, as they are labour and time intensive. Furthermore, the ALT can be estimated through modelling, using remotely sensed degree days of thaw or other factors (Sazonova and Romanovsky 2003; Zhang 2014). Modelling allows large-scale investigations, yet the spatial resolution is limited to km-scales and the result characterized by large uncertainties (Jia et al. 2017).

Recent studies have applied a new method based on ground subsidence to estimate the ALT. Ground subsidence occurs during the seasonal thawing period, due to the phase transition from ice to water in the soil pores of the active layer and the resulting volume change (Liu et al. 2012). The subsidence can be monitored remotely with the differential interferometric synthetic aperture radar technique (DInSAR). The technique is based on a SAR-image pair and uses the differences in the phase of the returning radio signal at the satellite sensor to map ground deformation between the image acquisition dates (Braun and Veci 2020). With the monitored ground subsidence, it is possible to derive the ALT change by considering the ice content in the soil pores. The ice content can be estimated through combining the soil saturation fraction (saturation of soil pores) with the soil porosity. Based on the volume change of ice to water it can be derived how much ice must have melted to water, to cause the monitored subsidence.

Knowing the ice content of the soil it can then be estimated how much the ALT changed over the monitored subsidence period.

The application of this method through remote sensing approaches would benefit current permafrost monitoring by allowing observations of the ALT at high temporal and spatial resolution.

1.1 Study aim

The aim of this thesis is to evaluate the ability of the ground subsidence method to estimate the maximum ALT and ALT development in Zackenberg, NE Greenland for the year 2017. The evaluation is based on field measurement comparison and the analysis of the ALT distribution, taking environmental factors into consideration.

1.2 Hypotheses

1. The estimated ALT from the remotely sensed ground subsidence is statistically similar to measured ALT (Liu et al. 2012)
2. Ground subsidence is largest in water-saturated areas and lowest in areas with low saturation fraction, due to the larger amount of ground ice in saturated upper soil layers (Daout et al. 2017; Chen et al. 2020).
3. The ALT will be largest on south-facing slopes, as the high insolation there enhances thawing (Liu et al. 2012; Gao et al. 2016).
4. The ALT will be smallest in Fens (peat-rich wetlands), where the peat layer allows large amounts of ground ice formation and insulates the ice from thawing, which significantly slows the thawing progress (Elberling et al. 2008; Atchley et al. 2016; Gao et al. 2016)
5. ALT error will be largest in areas with low saturation fraction, as the result here is most sensitive to a precise estimation of soil moisture and subsidence (Liu et al. 2012).

2 Background

2.1 Active layer dynamics

The AL results from the heat and moisture exchange between atmosphere and permafrost. Whilst the permafrost remains at temperatures below 0 °C throughout the year, the air temperature at the surface varies strongly throughout the seasons and thereby the AL functions as a transition zone (Fig. 1). The uppermost permafrost marks the permafrost table and the uppermost frozen part of the active layer is the frost table. The depth difference between the frost table and soil surface is defined as active layer thickness, yet this thaw depth is also known as active layer depth (Zhao et al. 2000; Woo 2012).

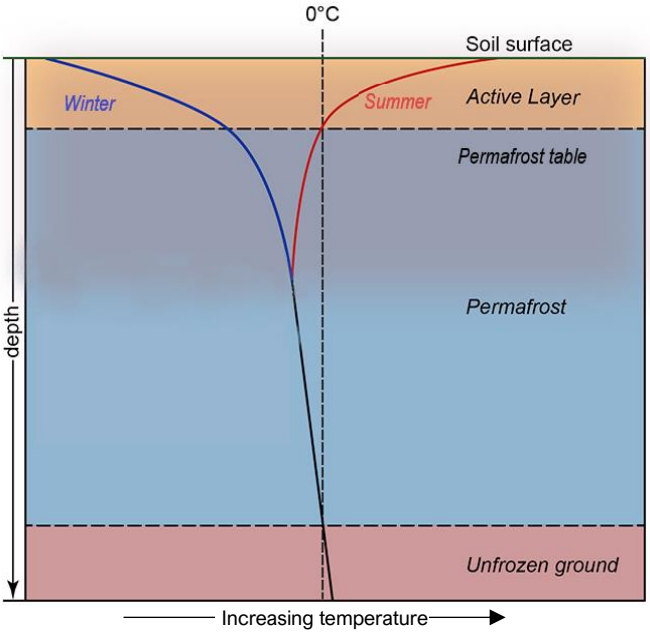

Figure 1: *Permafrost soil schematic with soil temperature vs depth, showing summer (red line) and winter (blue line) temperature variations. Adapted from CEN (2020).*

The development of the active layer throughout the year can be divided in four stages (Boike et al. 1998; Zhao et al. 2000; Wang et al. 2017):

a) Summer thawing stage:
After all snow has thawed, the AL is exposed to heating from the atmosphere and starts to thaw downwards. The heat flows are both conductive and nonconductive. In the upper thawed AL the moisture is evaporating, yet in the lower thawed AL the soil moisture is moving downwards to the freezing front.

b) Autumn freezing stage:
The period from maximum ALT to refrozen AL is often divided: first unidirectional freezing upwards from the permafrost table and then freezing from both the permafrost table upwards and from the surface downwards occurs. In both cases, soil moisture migrates from the thawed part towards the freezing front and thereby transfers heat in the AL. As a result, the temperature gradient decreases.

c) Winter cooling stage:
The AL is completely frozen and the temperature gradient across the AL reverses to colder temperatures at the soil surface with increasing temperatures towards the permafrost table. The temperature gradient is often steep, and conductive heat flows dominate the heat exchange. Snow cover can decrease the cooling of the AL, due to its insulating effect.

d) Spring warming stage:
With increasing air temperatures the temperature gradient in the AL reverses, as now the soil surface is warmer than the permafrost table. The main heat flow is conductive, yet moisture also migrates towards the warmer surface, where it evaporates. Snow can slow the warming of the AL, as it insulates the AL until the snow layer is thawed.

Of these stages, the summer thawing stage is especially important to explain the AL dynamics during the investigated thawing period in this thesis. In addition, the autumn freezing and spring

warming stages are of relevance due to the processes of moisture migration in the AL. This indicates varying ice content in the AL (Schuh et al. 2017; Wang et al. 2017).

The interannual ALT development has been found to strongly correlate with the mean annual air temperature (MAAT), snow depth and the seasonal thawing degree-day sums (Brown et al. 2000; Zhang 2005; Jorgenson et al. 2010).

Further, the active layer is significantly affected by local environmental factors and therefore varies on the scale of a few metres (Nelson et al. 1999; Brown et al. 2000; Wright et al. 2009). Important local factors are:

a) Soil characteristics:
   The soil type governs the local ALT because soil texture and composition influence thermal conductivity and porosity. The porosity determines the maximum water content and thereby the ice content the soil can hold. The thermal conductivity of soil increases with volumetric water content, yet the higher the ice content, the more thermal energy is required to thaw the soil column (Jorgenson et al. 2010). An important aspect is further the depth of the organic layer, which acts as insulation and has a very high porosity and thereby slows the thawing progress (Brown et al. 2000; Atchley et al. 2016).
b) Topography:
   The topography influences the surface energy balance through the impact of aspect and slope on the amount of incoming radiation (insolation). Areas on north-facing slopes receive less insolation than south-facing slopes, which can decrease the ALT (Gao et al. 2016). Another factor is that north-facing slopes and depressions have, as a result of the decreased insolation, a prolonged snow cover into summer, which further insulates the AL from thawing due to the high albedo and low thermal conductivity of snow (Zhang 2005). Also, elevation influences summer and winter air temperatures with higher elevations being characterized by lower ALT (Jorgenson et al. 2010). Additionally, the topography controls the local hydrology and thereby affects the water content of the soil.
c) Hydrology:
   The local hydrology is of importance because of the ability of water to transport heat. Thereby, local hydrology affects the depth of the permafrost table and the water content in the AL, with riverbeds and floodplains often showing very large ALT (Woo 2012). Furthermore, standing water in depressions can take up and store significant heat energy due to its low albedo (Jorgenson et al. 2010).
d) Microclimate:
   Variations in MAAT, wind and insolation interact with the other local factors. Wind can redistribute snow and thereby cause exposure or insulation of the AL (Zhang 2005).
e) Vegetation:
   The vegetation acts as insolating layer and it also influences the depth of the insolating organic layer. Absence of vegetation allows a stronger response of the AL to atmospheric conditions, which causes a stronger cool-down during winter and can allow faster thawing during summer (Woo 2012).

Based on these dependencies of the ALT distribution to the environmental parameters, the estimated ALT in this study should align to the study hypothesis in order to prove the applicability of the ground subsidence method. By focusing on southern aspects and Fen areas in the hypothesis, the ALT estimate distribution will be tested for plausibility regarding the effect of the organic layer thickness, ice content and insolation received (Jorgenson et al. 2010; Atchley et al. 2016).

2.2 Ground subsidence and the DInSAR method

To derive the ground subsidence, the differential interferometric synthetic-aperture radar (DInSAR) was applied. This radar-technique is used to map ground deformation by comparing two or more radar images.

Radar remote sensing uses radio-waves and is an active remote sensing technique. Successive radar waves are emitted to illuminate the scene and the echo is recorded by the sensor. The sensor does not only record the intensity of the backscatter, but also the part of the wave (phase) that hits the sensor. The phase (Φ) describes the exact position within one wavelength and can therefore range from -π to π (Fig. 2).

As the sensor records the phase, it is possible to compare the phase recorded in images at different times but the same location (repeat pass). Then, the difference in the recorded phase between the recordings can be derived if the topography is known (Fig. 2). If ground deformation occurred between the first and second pass the recorded phase for the individual pixel will not be the same, known as phase shift. The map showing the phase difference between the two acquisitions for each pixel is called interferogram and displays the phase difference within one radar wavelength from -π to π (Fig. 2). This method is called DInSAR (Moreira et al. 2013).

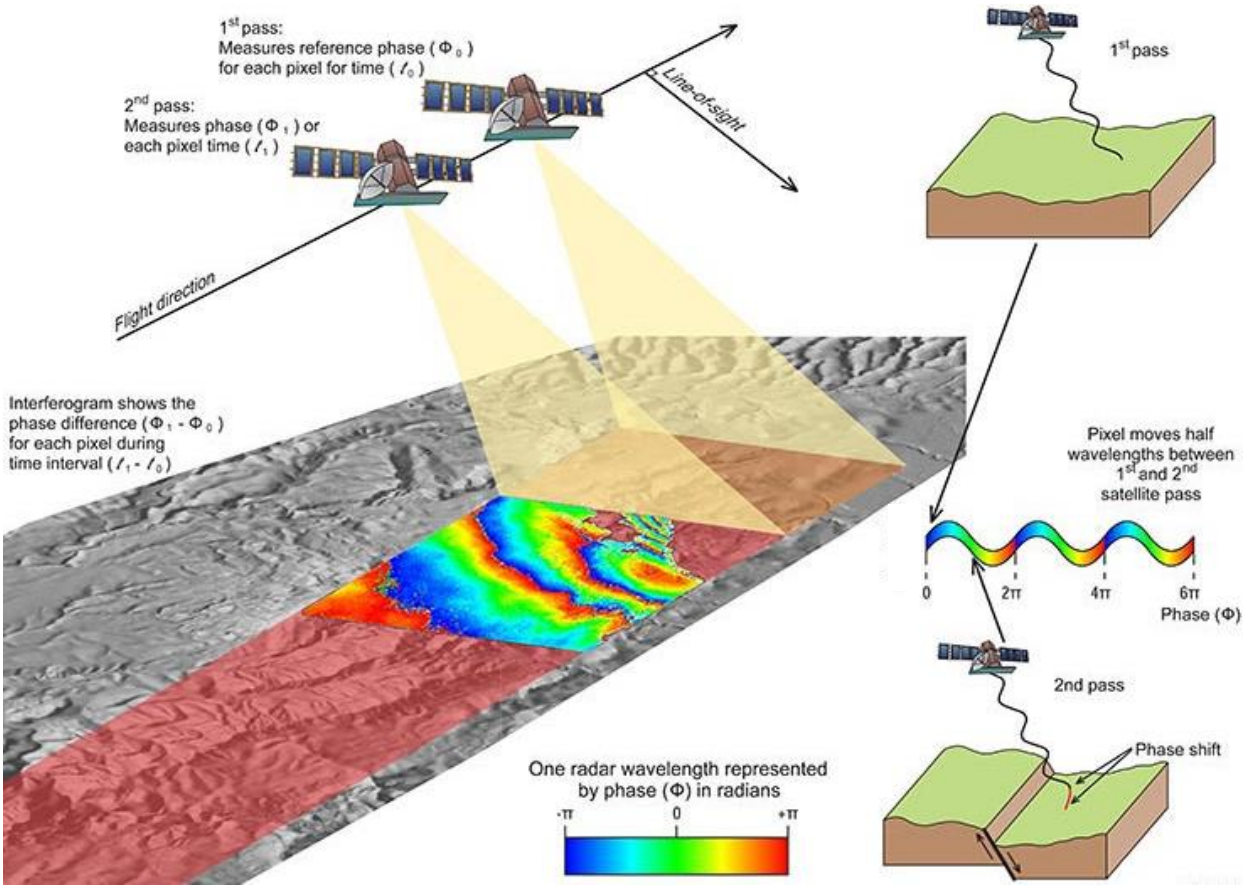

Figure 2: *Illustration of DInSAR method with two observations from different times and the recorded phase difference, adapted from Jaya et al. (2020).*

To obtain an accurate interferogram of the phase difference caused by surface displacement, all other contributing factors to the phase difference have to be excluded:

$$\Phi = \Phi_{DEM} + \Phi_{flat} + \Phi_{disp} + \Phi_{atm} + \Phi_{noise} \quad (1)$$

These other factors include the flat-earth phase Φ_{flat} (caused by Earth's curvature), the topographic phase Φ_{DEM} (caused by local topography), changes in atmospheric conditions Φ_{atm} (e.g. pressure, temperature, humidity), as well as other noise contributions Φ_{noise} (e.g. change in surface properties altering signal scattering).

The flat-earth phase can be removed with exact information on the orbit. Using a high-resolution DEM, the topographic phase can also be removed. The noise and atmospheric contribution can be kept small by decreasing the distance (spatial baseline) between the satellite position on the first and second pass, but they are difficult to model and remove (Braun and Veci 2020).

If these steps are considered, the resulting phase difference due to surface deformation can be evaluated for the quality of the phase information using a coherence estimate. The coherence shows how similar the phase information of the two compared images is and ranges from 0 – 1. If the coherence is low, influence of temporal, geometric or volumetric decorrelation can be assumed. Therefore, coherence thresholds are commonly applied to assure valid deformation results (Abe et al. 2020; Reinosch et al. 2020).

The final interferogram shows the phase difference within the scale of -π to π (Fig. 2). The phase difference therefore has to be integrated between neighbouring pixels (unwrapping) to receive a continuous raster. This is commonly done using specific algorithms (Chen and Zebker 2002).

The unwrapped phase difference can then be calculated into a displacement using the wavelength of the radar signal. As the radar antenna is slightly right-facing (Sentinel-1), the displacement has to be corrected from Line-of-Sight displacement to vertical displacement by considering the incidence angle. The resulting formula is:

$$D_{vertical} = \frac{(\Phi_{unwrapped} * \lambda)}{(-4 * \pi * \cos(\alpha_{incidence}))} \quad (2)$$

where $D_{vertical}$ is the vertical displacement, $\Phi_{unwrapped}$ is the unwrapped phase, λ is the wavelength of the radar signal and $\alpha_{incidence}$ is the incidence angle of the radar signal on the ground in radians (Short et al. 2014). For this transformation, it is of importance that no horizontal displacement exists (Abe et al. 2020).

The displacement map between the two images is then corrected for geometric SAR distortions caused by the topography. Thereby, errors caused by the interplay of incidence angle and local topography on the backscatter are corrected and the image is geocoded into a projected deformation map.

Lastly, the projected deformation map has to be tied to at least one ground control point, for which either deformation measurements can be used or a stable ground control point (Liu et al. 2012).

2.3 Previous studies

The DInSAR method has been widely used for monitoring of ground subsidence related to earthquakes or landslides (Moreira et al. 2013). However, for monitoring of ALT the method was first applied in 2012 by Liu et al. and used to monitor seasonal and multi-seasonal ALT developments at the North slope in Alaska (Fig. 3). This area is characterized by saturated soil and the resulting ALT was within the range of the variability found at field measurement sites. The authors estimated that the method is most sensitive to errors in the subsidence estimate, yet that with decreasing soil moisture the sensitivity to the correct determination of the soil properties (porosity and saturation) becomes more important (Liu et al. 2012).

The method was afterwards applied across several sites in the Qinghai-Tibet Plateau (Fig. 3). To estimate the ground ice content, the saturation fraction was either modelled (Wang 2018, Zhang 2020) or a constant value was used (Jia 2017). One study also estimated the ALT based on the time lag between maximum subsidence and maximum surface temperatures (Li 2015).

In the context of these studies, it will be of interest to evaluate how the method performs in an area of varying soil conditions and to evaluate the result by also using environmental parameters besides field measurements.

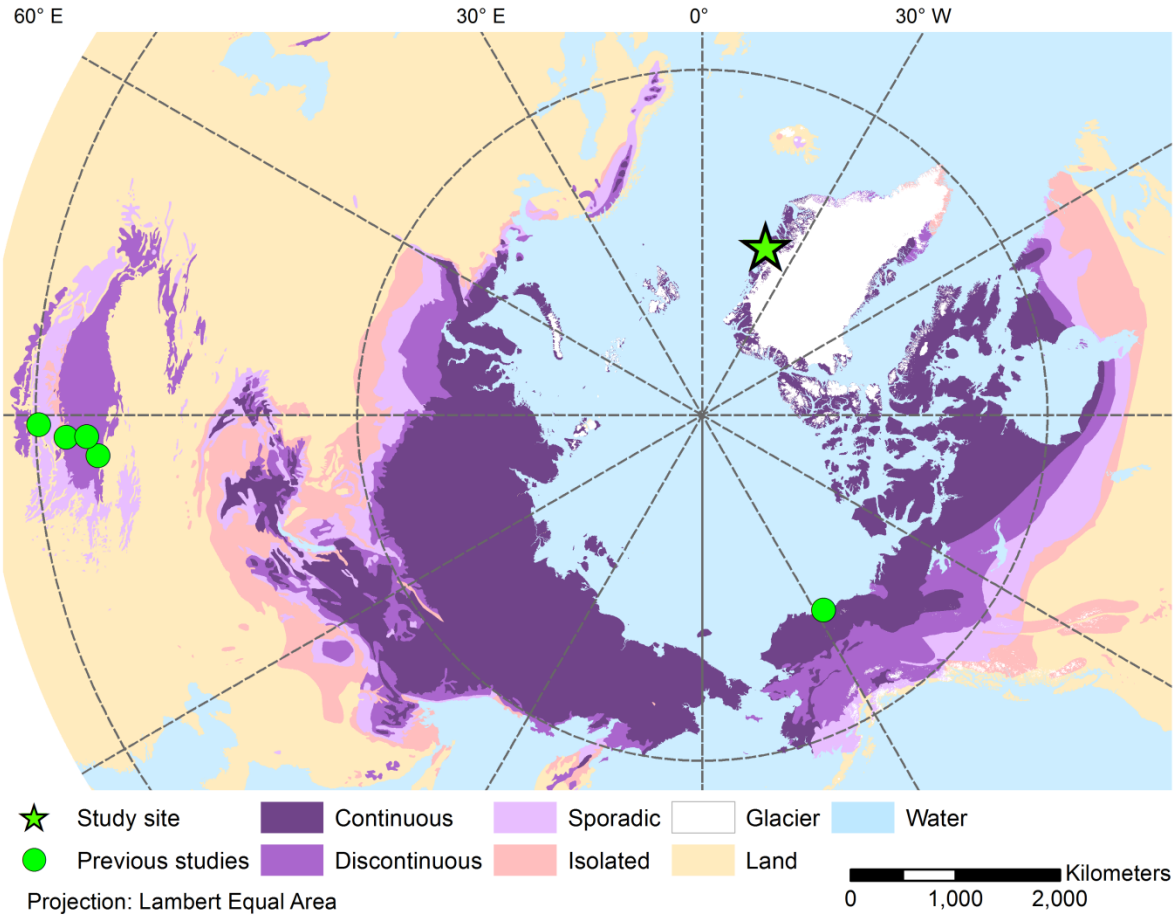

Figure 3: *Previous studies conducted on ALT estimates from DInSAR (Liu et al. 2012; Li et al. 2015; Jia et al. 2017; Wang et al. 2018; Zhang et al. 2020) with study site Zackenberg. Permafrost distribution from Brown et al. (2002) as background, which is based on permafrost coverage (continuous = 90-100 %, discontinuous = 50-90 %, sporadic = 10-50 %, isolated = 0-10 %).*

3 Methodology

3.1 Study site

The ALT was estimated for Zackenberg valley, which is located in NE-Greenland (74º28' N, 20º34' W) and lies within the region of continuous permafrost. The permafrost thickness is estimated to be 200 - 500 m across the valley (Christiansen et al. 2008).

The climate is high Arctic with an average annual temperature of – 9 °C and a mean annual precipitation of 260 mm (reference period: 1996 – 2005). Precipitation falls to 90 % as snow, and therefore the spatial distribution of snow governs the soil moisture content during the snow-free summer period (Hansen et al. 2008).

The valley has a diverse geomorphology, with the western side of the Zackenberg river characterized by gneissic bedrock and the eastern side being of sedimentary origin (Elberling et al. 2008).

About 65 % of the valley is vegetated by low-growing vegetation (Elberling et al. 2008). Barren areas result from exposed bedrock or wind erosion (Rasmussen et al. 2018). The drier parts of the valley are inhabited by heather species, such as Dryas (*Dryas integrifolia*) and Cassiope (*Cassiope tetragona*). Areas of long-lasting snow coverage are often vegetated by Salix (*Salix arctica*) and wetter areas are covered by Grassland (e.g. *Arctagrostis latifolia*) and Fen (e.g. *Eriophorum scheuchzeri*) vegetation (Elberling et al. 2008).

The chosen study area extends over 46.84 km² and covers the main valley to an altitude of 200 m (Fig. 4). Areas above this altitude were excluded to reduce the influence of slope movements on the subsidence result (Fuhrmann and Garthwaite 2019).

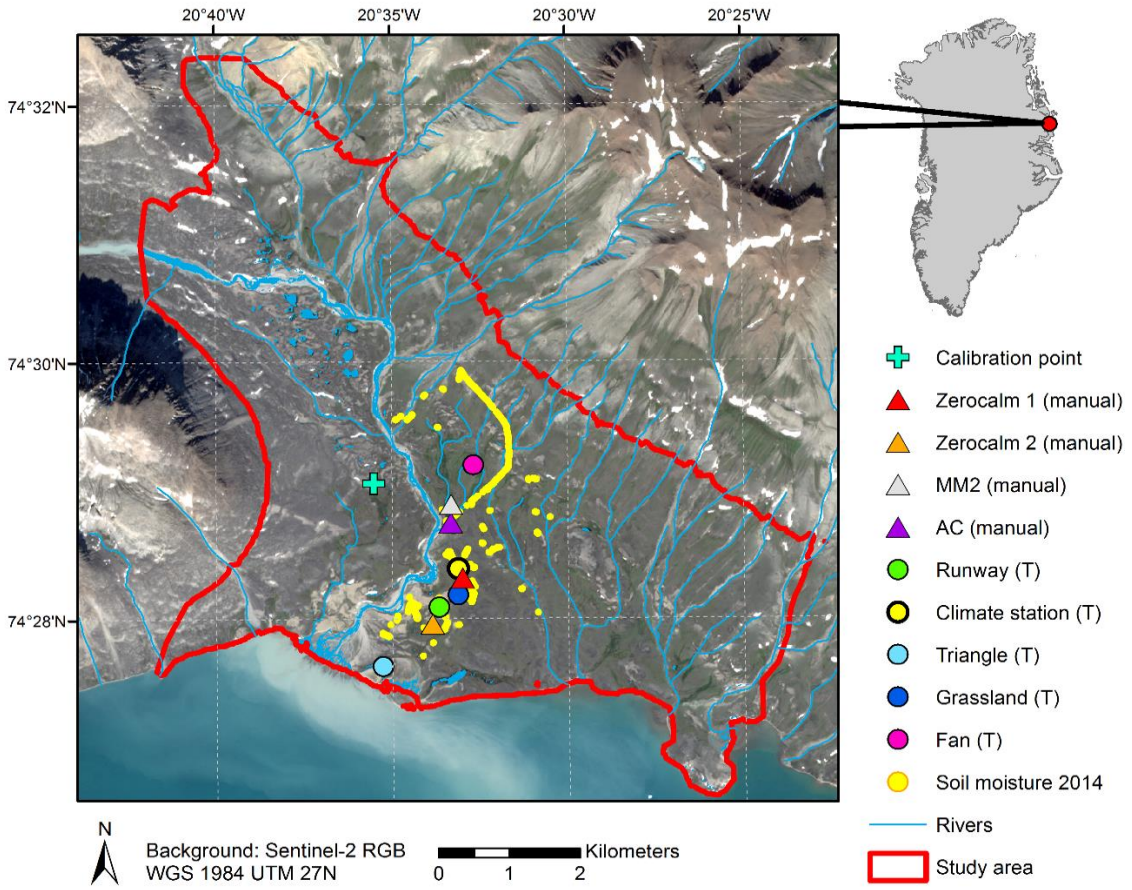

Figure 4: *Study area with field measurement points (manual = manual ALT probing; T = thermistor string measuring temperature with sensors in 0.25 m depth intervals).*

3.2 Data and processing environment

Sentinel-1 SAR scenes for the subsidence mapping were retrieved from the Copernicus Open Access Hub website (Table A1). The processing of the subsidence mapping was performed in SNAP Version 7 (Sentinel Application Platform, Version 7.0.4, ESA, Paris, France) with the use of the SNAPHU-Unwrapping plug-in (Chen and Zebker 2002).

The data for the porosity and saturation fraction was obtained from varying sources (Table A1) and together with the subsidence results processed in ArcMap 10.5 (ESRI, Redlands, California). All layers were clipped to the extent of the defined study area (Fig. 4) and projected into the coordinate system WGS 1984 UTM 27.

For further information on the data sources, see Table A1.

Field measurement data was received through the Greenlandic Ecosystem Monitoring program from GeoBasis Zackenberg and ClimateBasis Zackenberg (GEM 2020a). The processing of these measurements was accomplished in Microsoft Excel 2010 (Microsoft Corporation, Redmond, Washington).

The statistical evaluation of the results was conducted in MATLAB (Version 2017b, Natick, Massachusetts: The MathWorks Inc.) and a spatial autocorrelation test (Global Moran's I) was performed using ArcPy in ArcMap 10.5 (ESRI, Redlands, California).

3.3 Active layer thickness estimation

In order to estimate the ALT based on the ground subsidence throughout the thawing season 2017 several variables had to be derived (Fig. 5).

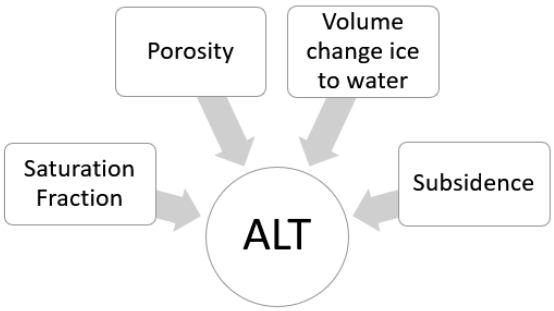

Figure 5: *Scheme of parameters used for the estimation of ALT change based on Liu et al. (2012).*

The ground subsidence was obtained with the DInSAR technique and by estimating soil porosity and soil saturation, the ice content was derived across the study area. With these variables, the ALT change during the subsidence period can then be calculated using:

$$\Delta H = \delta \frac{\rho_{ice}}{PS(\rho_{water} - \rho_{ice})}, \quad (3)$$

where ΔH is the change in active layer thickness (in meters), δ is the subsidence (in meters) and ρ_{ice} and ρ_{water} are the density of ice and water respectively (in kg/m³). P is the porosity (as decimal) and S the saturation fraction (as decimal). Together they represent the ice content of the frozen active layer (Liu et al. 2012).

The derivation of these variables is explained in the following sections.

3.3.1 DInSAR subsidence

To determine which period was to be evaluated with the DInSAR method, the thawing period was extracted from field measurements of five thermistor strings (GeoPrecision GmbH, Ettlingen, Germany). These strings measure temperature in 0.25 m depth intervals. The thawing start was defined as the date where the mean daily 0 cm soil temperature had first reached 0.1 °C. In this way, the time period at which the temperature levelled at 0 °C for the snow melt was excluded. The thawing end was defined as the point when the soil started to freeze upwards from the permafrost table (Zhao et al. 2000; Wang et al. 2017).

The thawing period determined by the thermistor evaluation spanned from 08-06-2017 to 31-08-2017 (Fig. 6; Fig. A8).

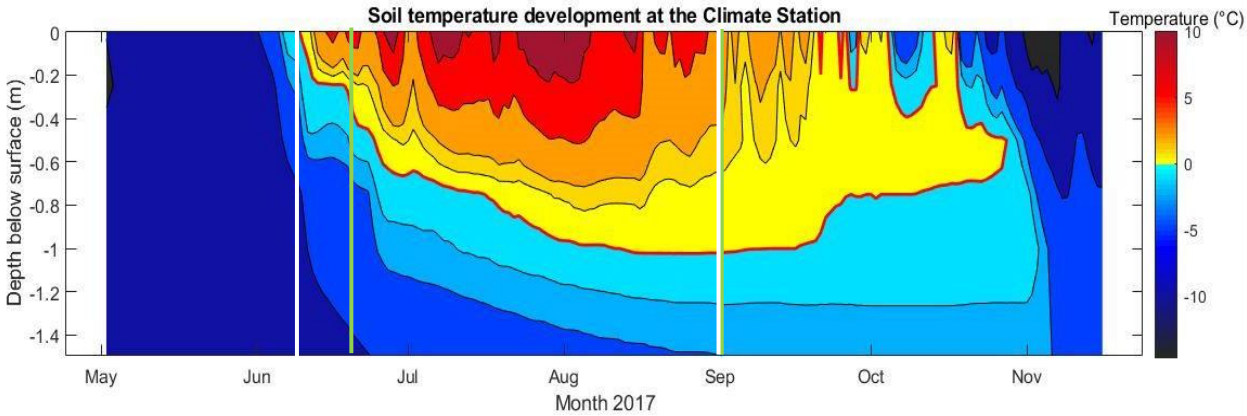

***Figure 6**: Daily mean soil temperatures at the Climate Station for May to November 2017 with red line showing 0 °C isotherm, white lines showing thawing period and green lines DInSAR period.*

Sentinel 1-Synthetic aperture radar images (SAR-images) for every 12th day during this period were acquired (Table A2). The SAR-images are available for every 6th day, but a 12-day interval was chosen to decrease the processing time, whilst still limiting coherence loss caused by temporal change of the scatterers (e.g. vegetation growth).

The subsidence analysis was conducted between each successive image pair (e.g. 1st SAR-image & 2nd SAR-image, 2nd SAR-image & 3rd SAR-image etc.). For the subsidence processing, a 5 m-DEM (Table A1) was used and the phase difference was unwrapped using the SNAPHU plugin (Chen and Zebker 2002). The resulting displacement was converted from Line-of-Sight displacement to vertical displacement using the cosine of the incidence angle (Equation 2). As the SAR-images used in this study were taken by the Sentinel-1A satellite, a wavelength of 0.053 m (ESA 2020) was used. The resulting subsidence was filtered for a sufficient coherence threshold of 0.3 to decrease noise (Abe et al. 2020; Reinosch et al. 2020).

Due to insufficient coherence, the first SAR-image had to be excluded, as less than 50% of the calculated subsidence in the study area had a coherence above the chosen threshold. Therefore, the period with data on the subsidence changed to the time period 20-06-2017 to 31-08-2017.

The subsidence was calibrated with a zero-subsidence point in the valley. This calibration point was chosen by finding the cell across the valley with the highest coherence over all image pairs (coherence = 0.93) (Liu et al. 2012). Each subsidence image was then interpolated for missing subsidence raster cells due to insufficient coherence by applying the Elevation-Void-Fill tool in ArcGIS, which applies inverse distance weighted interpolation.

All subsidence images were summed up to derive the total subsidence (flow chart: Fig. A1).

3.3.2 Estimation of porosity

The soil at Zackenberg is mineral soil with varying amounts of organic matter (Elberling et al. 2008). The porosity was estimated for 0 – 1 m soil depth based on mineral soil porosity and organic soil porosity (for flow chart see Fig. A2).

The porosity of the mineral soil part was estimated using the sand fraction, following an empirical formula from Cosby et al. (1984). The formula was derived through the analysis of over 1100 soil samples and relates mineral soil porosity to the sand fraction only:

$$P_{mineral} = 0.489 - 0.00126 * frac_{sand} \quad (4)$$

The sand fraction was determined using sand weight per volume and bulk density at 250 m resolution (ISRIC 2020a).

To estimate which fraction of the upper meter of soil is organic, field measurements of carbon density results from Palmtag et al. (2018) were evaluated for simplified geomorphological classes (Table A4; Cable et al. 2018). The carbon density was divided by the carbon density of peat, which is assumed to be 100 % organic matter. A peat carbon density of 140 kg/m^3 was used (Liu et al. 2012). The resulting organic fraction was assigned the porosity 90 % based on the porosity of peat (Rezanezhad et al. 2016).

To derive the overall porosity the organic and mineral porosity was combined using:

$$P = ((1 - frac_{org}) * P_{mineral}) + (frac_{org} * P_{org}) \quad (5)$$

3.3.3 Estimation of saturation fraction

The saturation fraction across the valley was estimated in order to approximate the ice volume in the soil during the thawing season of 2017. The estimate was based on the saturation at the end of the thawing season of the previous year, 2016, and derived by combining a soil moisture index and in-situ measurements (for flow chart see Fig. A2).

Different soil moisture indices (Topographical Wetness Index, Normalized Difference Water Index, Normalized Soil Moisture Index) were tested for significant correlation to extensive soil moisture measurements from 2014 (Table A1). The indices were calculated based on the 5 m-DEM or based on a Sentinel-2 image from the 12-08-2016 (Table A5). The date was chosen as a mean of the time of the soil moisture measurements (mid of July) and the start of the soil freeze-up (end of August) while considering cloud-free acquisition conditions.

The soil moisture data was averaged for grid cells of the same resolution of the Sentinel-2 image (20 m), resulting in 358 grid cells with soil moisture data.
The Normalized Soil Moisture Index (NSMI) showed the most significant result ($p < 0.00001$) (Table A3) and the following function with an r^2 of 0.64 was used to relate the NSMI to soil moisture across the study area using a simple regression (Fig. 7):

$$soil\ moisture = 185.83 * NSMI - 8.2639 \quad (6)$$

The NSMI is calculated as (Haubrock et al. 2008):

$$NSMI = \frac{R\,(1800\,nm) - R(2119nm)}{R\,(1800\,nm) + R\,(2119nm)} = \frac{Band_{11} - Band_{12}}{Band_{11} + Band_{12}} \text{ (for Sentinel)} \quad (7)$$

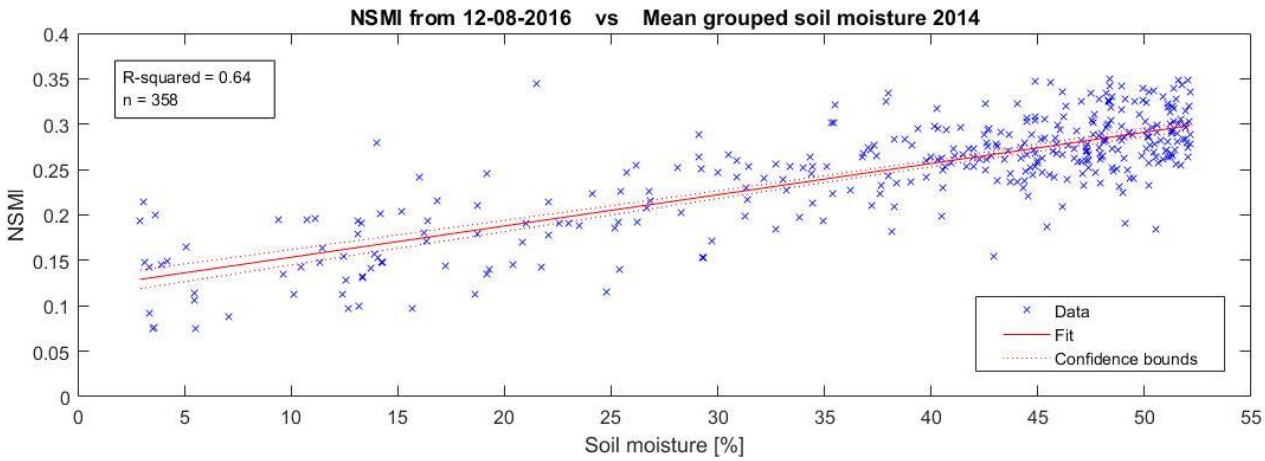

Figure 7: *NSMI vs. soil moisture measurement correlation. The linear trendline (red) with 95 % confidence bounds describes the used NSMI-soil moisture relationship.*

The soil moisture calculated based on the NSMI was considered to represent the upper part of the soil, as the NSMI is based on the surface reflectance, which is influenced by the topsoil saturation (Haubrock et al. 2008). The soil moisture was converted to saturation fraction (%) by dividing the local soil moisture by the local porosity. This saturation fraction was assumed to represent the mean saturation fraction of the uppermost soil. As the permafrost table has been found by other studies to act like a drainage barrier, and thus creates saturated water conditions in the lower AL (Wang et al. 2017; Wang et al. 2018), this had to be considered for the mean saturation fraction estimate across the AL. The permafrost table was assumed to be at 1 m depth, based on the majority of measured ALT being less than 1 m (Fig. 8). In addition, Christiansen et al. (2008) modelled the ALT across the valley and derived ALT in the range of 0.5 to 0.8 m. Nevertheless, the assumed constant permafrost table depth at 1 m depth is a strong simplification. To adjust the saturation fraction for the saturation at the permafrost table, all areas with a NSMI saturation fraction S_{NMSI} above 50% were adjusted to the mean of 0.5 m saturated soil and 0.5 m S_{NMSI} content:

$$S = (100 * 0.5) + (S_{NMSI} * 0.5) \quad (8)$$

Areas with an S_{NMSI}below 50% were assumed to be less saturated also deeper down in the soil and therefore a linear function was applied, which increased the saturated fraction linear to the NSMI saturation fraction:

$$S = (S_{NMSI}) + ((1 - S_{NMSI}) * S_{NMSI}) \quad (9)$$

According to this, the saturation fraction was adjusted. The threshold chosen aligns with in-situ measurements of Hollesen et al. (2011) and Rasmussen et al. (2018), which showed saturated conditions below 0.5 m depth at the station Zerocalm-1 in Zackenberg valley.

3.3.4 Active layer thickness calculation

The ALT was calculated by combining the derived saturation fraction, soil porosity and subsidence through equation 3.

The maximum ALT was obtained by using the total subsidence, and the progression throughout the thawing season was calculated by using the individual subsidence for each 12-day period.

As the analysis period only included the subsidence starting from 20-06-2017, the measured ALT progression until then was added to the result for each station (for flow chart see Fig. A3).

The estimated ALT will further be referred to as ES-ALT.

3.4 Field measurements of ALT

3.4.1 Processing

Field measurements for 2017 were available from nine sites (Fig. 4, Table 1). This included manual probing measurements of active layer depth from two sites connected to the Circumpolar Active Layer Monitoring Network (CALM): Zerocalm-1 (ZC1) and Zerocalm-2 (ZC2). Additionally, data was available from two other manual probing sites (MM2 and AC). The manual probing is done by pressing a metal rod through the soil until the frost table is hit and measuring thereby the ALT. Further, temperature-depth measurements were available from five thermistor strings (GeoPrecision GmbH, Ettlingen, Germany) which were also used to investigate the thawing period (see section 3.3.1). These strings measure temperature at every 0.25 m depth.

Table 1: *Field sites and main characteristics. Vegetation type and soil moisture regime based on Elberling et al. (2008)*

Site	Measurement type	Vegetation type	Moisture regime
ZC1	Manual probing	Cassiope with parts of Salix	Drier
ZC2	Manual probing	Grassland with parts of Fen, Salix, Cassiope, Dryas	Moist
AC	Manual probing	Fen	Wet
MM2	Manual probing	Fen	Wet
Runway	Temperature	Salix	Intermediate
Climate St.	Temperature	Salix	Intermediate
Triangle	Temperature	Barrens	Very dry
Grassland	Temperature	Salix	Moist
Fan	Temperature	Fen	Wet

The manual probing measurements at ZC1 included data from 121 measurement points, which are located at 10 m distance to each other in a 100 m x 100 m grid. For ZC2 the manual probing measurements consist of 208 points at 10 m distance to each other over a 120 m x 150 m grid. The manual probing at AC include 8 points within a 2 m x 5 m area. For MM2 5 points along a 2 m transect are manually probed (Skov 2020).

For all manual probing sites, the point measurements were averaged for each site and date, with points covered by snow assumed to have 0 m ALT. If the measurements were not taken on a date that aligned with the analysed images, then the depth development was linearly interpolated to that date, based on the assumption of linear ALT increase.

The data from the thermistor strings were also evaluated for the depth of the freezing front, which was assumed to be at 0 °C (Zhao et al. 2000). The data of the two depths which were closest to the freezing front were linearly interpolated to find the depth of the 0 °C isotherm (Frauenfeld 2004).

The in-situ ALT based on the field measurements will in the following be referred to as M-ALT.

3.4.2 Resulting field measurement data

The maximum M-ALT at the manual probing Zerocalm sites in Zackenberg for the thawing season of 2017 was 0.83 m for Zerocalm-2 and 0.71 m for Zerocalm-1 (Fig. 8). The manual probing sites MM2 and AC, located in a Fen, recorded the lowest maximum M-ALT with 0.52 m and 0.56 m. The values of the temperature strings at the drier sites Triangle and Runway show the deepest maximum M-ALT with 1.2 to 1.5 m.

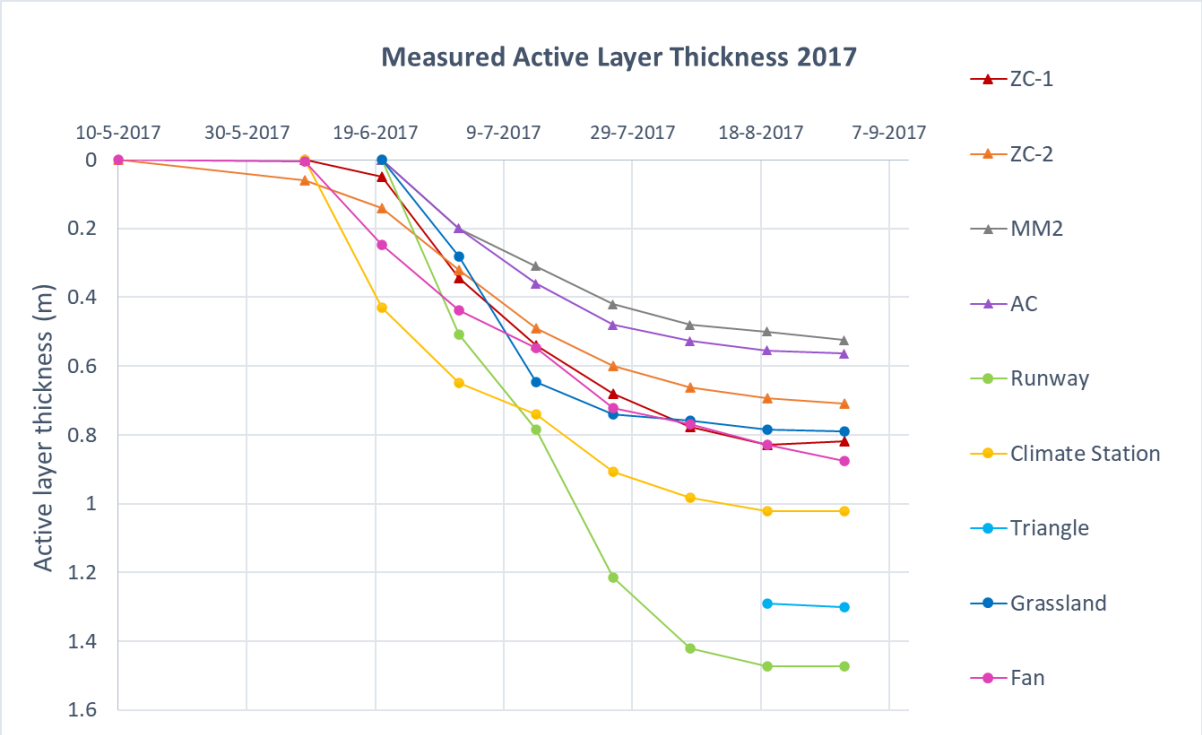

Figure 8: *Temporal development of in-situ active layer thickness during thawing season 2017 (Triangle markers indicate manual probing sites and circles indicate thermistor strings).*

3.5 Evaluation of estimated active layer thickness

In order to review the distribution of the used subsidence, the correlation between subsidence and NSMI-based soil moisture as well as the saturation fraction for 0-1 m soil depth was determined (hypothesis 2).

To evaluate the ES-ALT the total and successive ES-ALT change was extracted at each station. The ES-ALT and M-ALT was then compared, considering both the temporal development and maximum thickness (hypothesis 1). The difference of the ES-ALT to M-ALT was also correlated with the local saturation fraction (hypothesis 5).

The total ES-ALT distribution was further analysed for relationships to environmental parameters:

- Vicinity to streams
- Aspect (four major directions) (hypothesis 3)
- Bare vs. vegetated areas
- Vegetation type (hypothesis 4)
- Depressions vs. flat areas vs. slopes

For this, a Euclidian distance raster to streams, a reclassified aspect raster based on a 5 m resolution DEM and a reclassified vegetation raster (Elberling et al. 2008) were used (Table A2, Table A3, Fig. A5, Fig. A6). The depression values were estimated by applying the ArcGIS Fill tool on the 5 m resolution DEM and subtracting the initial DEM from the result. Thereby, only the local depressions remained, which were filtered for an area size above 50 m^2 to decrease noise potentially caused by DEM errors (Wechsler 2007). The depressions were then combined with a reclassed slope raster based on the DEM, where all slope values below 2° were assumed to be flat and all slope values above 2° were classed as slopes.

For the evaluation of the relationship to the environmental parameters, the ES-ALT raster data was bilinear aggregated to 50 m resolution in order to decrease the number of data points (n = 112000 vs. n = 18000). This was done to decrease possible exaggeration of the statistical significance of performed statistical tests as an effect of large sample sizes (Lantz 2013). Further, lakes and rivers based on Elberling et al. (2008) (Table A2, Fig. A5) were excluded.

To statistically evaluate the results, all data were tested for being normally distributed by evaluating the kurtosis and skewness of each variable. As the data did not meet the criteria of normal distribution, only tests applicable for non-parametric data were used (Kanji 2006):

- The one-sample Wilcoxon signed rank test was used to test if one sample belongs to a population with a known mean (Kanji 2006).
- The Wilcoxon rank sum test was applied when two independent samples were tested for belonging to the same population (Kanji 2006).
- The Kruskal-Wallis test was used to evaluate if several independent samples belong to the same population (Kanji 2006).
- The Spearman's rank correlation coefficient was applied to test for relationships between two samples (Kanji 2006).
- Regression analysis was used to relate one dependent variable to one or several independent variables (Kanji 2006).
- The Nash-Sutcliffe efficiency statistic (NSE) was applied to evaluate the agreement between observed and estimated ALT. The test compares the relative magnitude of the residual variance to the measured variance using the formula:

$$NSE = 1 - \frac{\sum_{t=1}^{T}(Q_e^t - Q_o^t)^2}{\sum_{t=1}^{T}\left(Q_e^t - \overline{Q}_o\right)^2} \qquad (10)$$

  where Q_o is the observed value, Q_e is the estimated value, t is the value at time t and T is the end time. A perfect fit is indicated by a NSE of 1, while values below 0 indicate that the observed mean is a better predictor of the temporal ALT development than the estimate (Nash and Sutcliffe 1970).
- The Global Moran's I statistic was used to test for spatial randomness. Based on a matrix of correlation coefficients the test measures the spatial autocorrelation (tendency of areas close together having similar values). The Moran's I index ranges between -1 and +1 and indicates the spatial dependency. The resulting p-value displays the likelihood of the data being randomly distributed and a z-score measures the dispersion / clustering compared to spatial randomness (Moran 1950).

All tests produce a p-value ranging from 0 to 1, which indicates the probability of the null hypothesis H0 (no difference / relationship between the samples) being true. The p-values were evaluated for a significance level α of 0.05, below which H0 was rejected (flow chart: Fig. A4).

4 Results

4.1 Derived soil moisture and porosity

The soil moisture based on the NSMI varied from 0 to 72 % for the topsoil, which led to oversaturation in some areas. These were corrected to a saturation fraction of 1. The derived saturation fraction then ranged from 0 to 1 for the soil from 0 - 1 m depth (Fig. 9A). This value is assumed to represent the average saturation when the soil froze in 2016 and thus represents combined with the porosity the ice content.

The derived organic fraction based on Palmtag et al. (2018) ranged from 0 to 23 % (Table A4). The mean carbon density used of 11.2 kg C /m² aligned to the range of 10 – 25 kg C / m² recorded by Hugelius et al. (2013). The calculated mean sand fraction of 43 % was within the range of fractions observed in other studies. Hollesen et al. (2011) determined a sand fraction around 80 % for 0 - 1 m depth at the Zerocalm-1 station, yet Morel et al. (2019) and Rasmussen et al. (2018) recorded lower values of 16.7 % (at AC station) and 30 % (at the Climate station) respectively. The calculated porosity ranged from 42 % to 58 % (Fig. 9B).

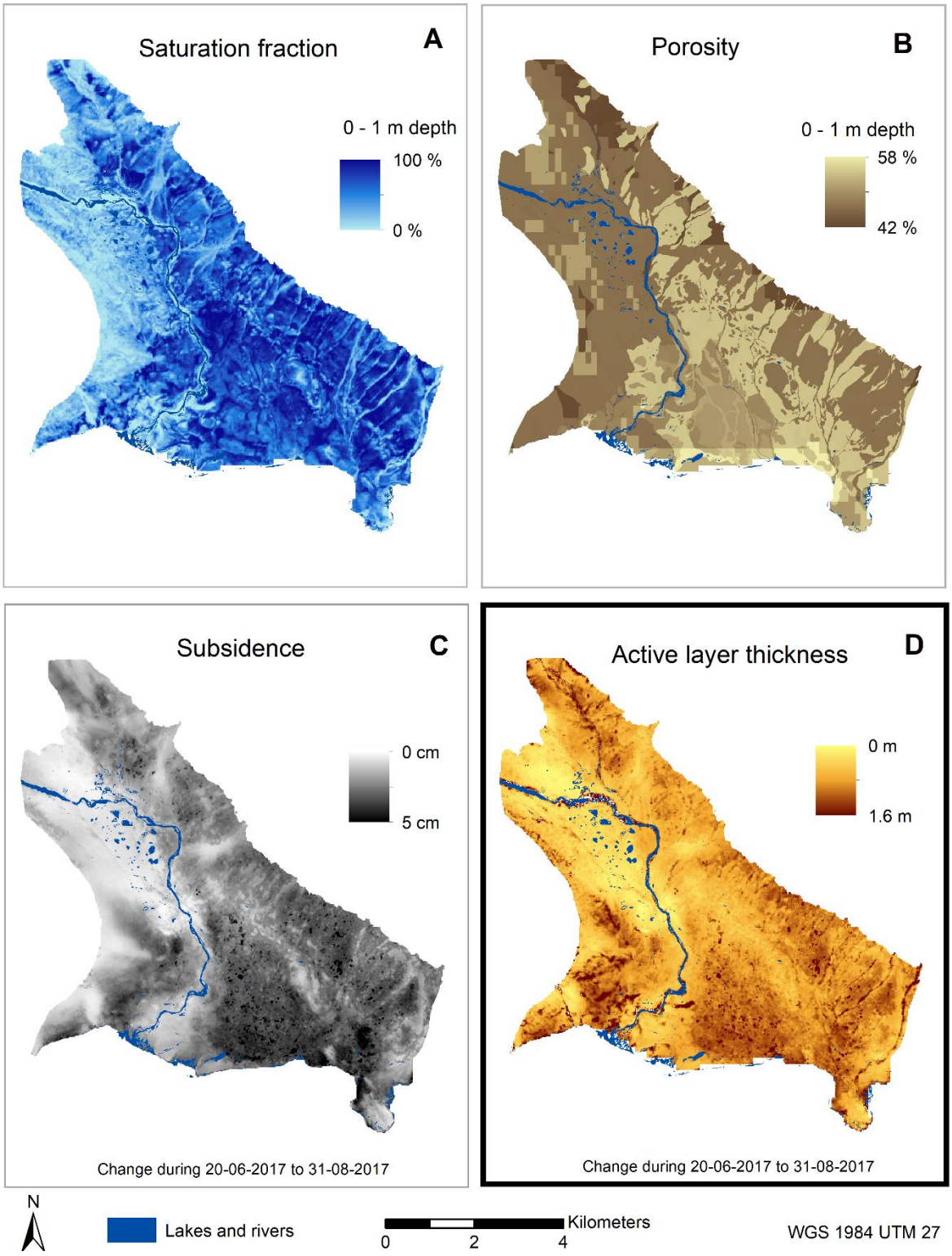

Figure 9: ***A*** *= Estimated saturation fraction for 0-1 m depth,* ***B*** *= Estimated porosity for 0-1 m depth,* ***C*** *= Total subsidence from 20-06 to 31-08-2017 based on DInSAR analysis,* ***D*** *= Estimated active layer thickness (ES-ALT) change from 20-06 to 31-08-2017.*

4.2 Evaluation of subsidence

Both the NSMI-based soil moisture and saturation fraction for 0 – 1 m soil depth are significantly correlated to the subsidence based on the Spearman's rank correlation coefficient (Table 2, Fig. 10). The relationship indicates that subsidence is lowest in drier areas. From subsidence larger than 0.03 m the correlation begins to slightly level out (Fig. 10). Nevertheless, hypothesis 2 of larger subsidence in water-saturated areas is supported.

Table 2: *Correlation of subsidence to NSMI-based soil moisture and saturation fraction across entire study area using the Spearman's rank correlation coefficient.*

Subsidence correlated to	Rho	P-value	Sample-size (n)
NSMI-based soil moisture	0.69	~ 0	18024
Saturation fraction	0.68	~ 0	18024

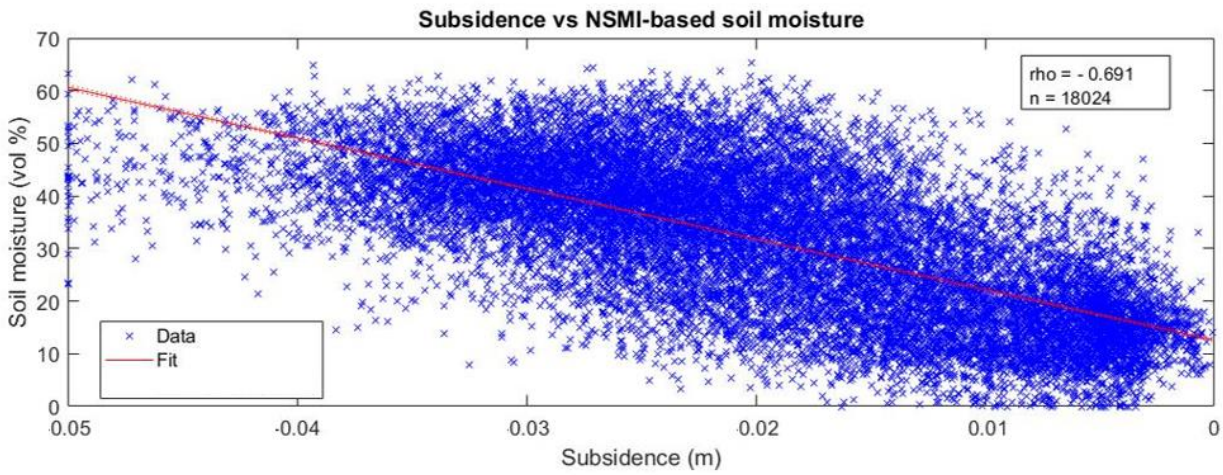

Figure 10*: Correlation of subsidence to NSMI-based soil moisture with Spearman correlation coefficient rho.*

4.3 Estimated active layer thickness

The mean total ES-ALT change across the study area for the analysed period (20-06-2017 to 31-08-2017) amounted to 0.63 m with a standard deviation of 0.28 m, indicating a large variability of the ALT.

The ES-ALT development throughout the thawing season follows the overall trend of increasing ALT. However, some time intervals show no increase in subsidence at some stations and sudden jumps in the following ES-ALT progression can be seen (Fig. 11).

Figure 11: *Temporal development of estimated active layer thickness at the field measurement stations during investigated period (20-06-2017 to 31-08-2017).*

4.4 Accuracy evaluation with field measurements

The results for the maximum ES-ALT based on the DInSAR method are compared against the M-ALT at each field measurement site in Fig. 12. Based on a Wilcoxon rank sum test the two samples are statistically similar (p-value = 0.55), which supports hypothesis 1. Nevertheless, it is clearly visible that the station 'Runway' is an outlier (the red bars in Fig. 12 show the differences between maximum ES-ALT and M-ALT), and the likelihood of similarity between M-ALT and ES-ALT increased to a p-value of 0.96 when the outlier was excluded. The mean absolute difference of the maximum ES-ALT compared to the M-ALT is 0.16 m (18 % of mean maximum M-ALT) and decreases to 0.07 m (9 % of mean maximum M-ALT) if the Runway station is excluded.

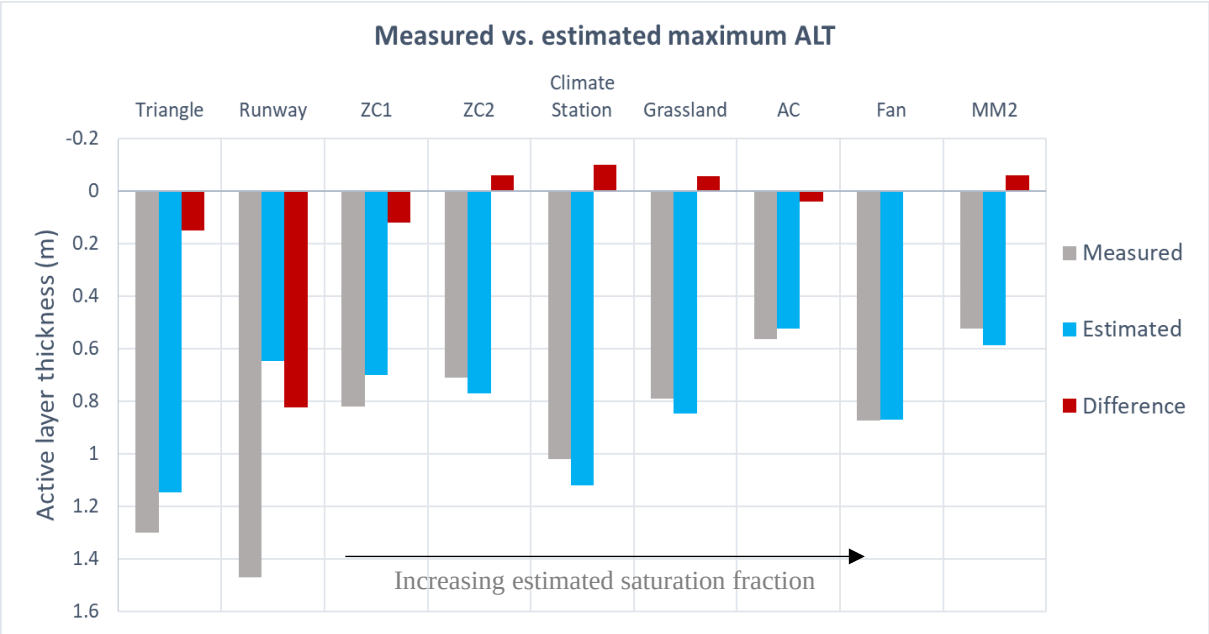

Figure 12: *Comparison of maximum ES-ALT (blue bars) and M-ALT (grey bars) including error display (red bars) based on M-ALT minus ES-ALT.*

Over the study period, the ES-ALT for each station was not exactly following the respective M-ALT, which would have been indicated by zero difference in the temporal development of the ALT (Fig. 13). The period of greatest offset aligns with the 12-day period when the ES-ALT progression had stagnated (14-07-2017 to 26-07-2017) (Fig. 11). Also, it is clearly visible that the ALT at the Runway station was strongly underestimated (Fig. 13). The mean offset of M-ALT minus ES-ALT over the entire period accounts to 0.13 m (0.07 m without the Runway), indicating that the ALT was under- rather than overestimated over time.

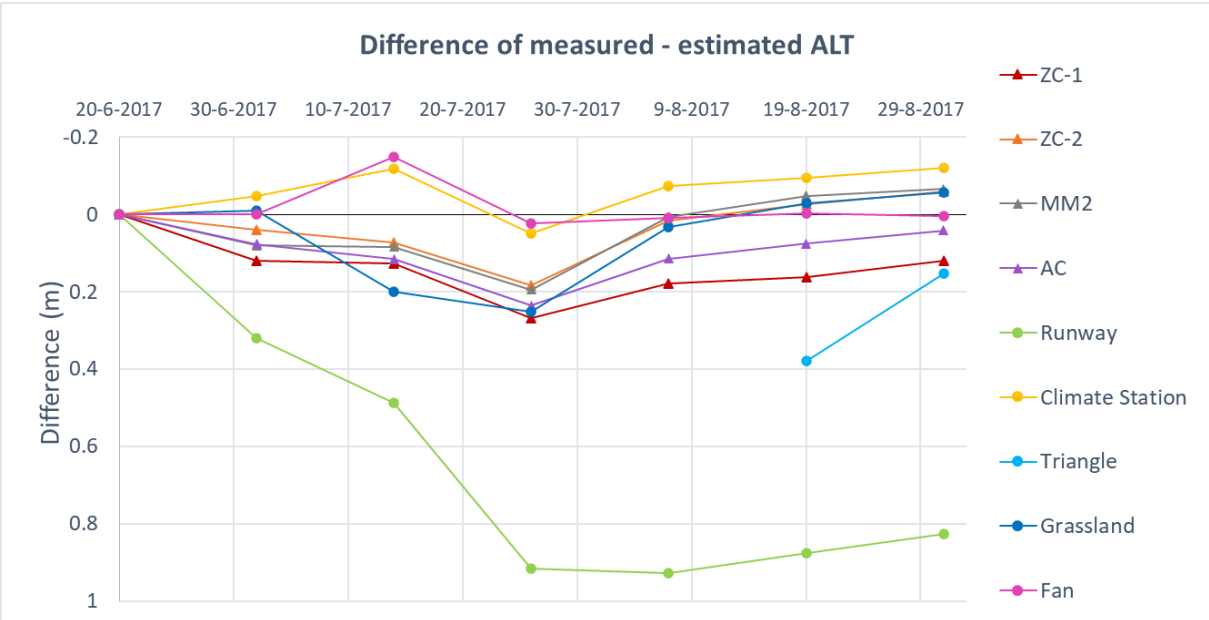

Figure 13: *Temporal development of difference between measured and estimated ALT during investigated period (20-06-2017 to 31-08-2017). The difference is based on M-ALT minus ES-ALT.*

The temporal development of the ES-ALT vs. M-ALT was evaluated by comparing the slope of the linear trendline between M-ALT and ES-ALT over time with the ideal fit (slope = 1). This was done for each station (Table 3). Using a one-sample Wilcoxon signed rank test, the difference to the ideal fit of 1 was statistically not significant (p-value = 0.33), even though the Runway station also clearly stands out here as an outlier. This supports hypothesis 1 of the ES-ALT being statistically similar to the M-ALT.

***Table 3**: Station-wise comparison of estimated vs. measured ALT development over study period.*

Station	n	Difference of linear slope to ideal slope (= 1)	NSE
ZC-1	7	0.20	0.66
ZC-2	7	-0.03	0.84
AC	7	0.15	0.66
MM2	7	-0.09	0.74
Runway	7	0.62	-0.80
Climate Station	7	-0.1	0.84
Grassland	7	0.07	0.81
Fan	7	0.04	0.94
Triangle	Excluded due to n = 2		

By applying the Nash-Sutcliffe efficiency statistic (NSE), it was tested if the ES-ALT at each time point had a better agreement to the respective M-ALT than the mean of the M-ALT. The result showed that all stations besides the Runway have a very high agreement, with 1 being the best possible fit (Table 3). The negative value of the NSE indicates that at the Runway station the mean of the M-ALT would have been a better predictor of the temporal development than the ES-ALT. Also this result supports hypothesis 1.

The absolute difference of the maximum ES-ALT to the M-ALT was tested for correlation to the saturation fraction at the station using the Spearman's rank correlation coefficient, and the difference was significant (ρ = -0.73, p-value = 0.03). This indicates that hypothesis 5 is supported, so the ES-ALT error increases in drier areas.

4.5 Accuracy evaluation with environmental parameters

The ES-ALT showed no correlation trend for the distance to the closest stream using the Spearman's rank correlation coefficient (ρ = 0.09, p-value ~ 0). This evaluation was based on comparing the distance to the nearest stream with the respective ES-ALT value over the entire study area at 50 m raster resolution.

Regarding the four major aspect directions, the ES-ALT differs significantly based on the Kruskal-Wallis test (p-value ~ 0) (Fig. 14). The largest ES-ALT with a mean of 0.67 m is found on south-facing slopes, whilst north-facing slopes have the smallest mean ES-ALT with 0.50 m. Comparing the southern aspect class to the merged other aspects with a Wilcoxon rank sum test the result is statistically different as well (p-value ~ 0). This supports hypothesis 3, that southern aspects are characterized by the largest ES-ALT.

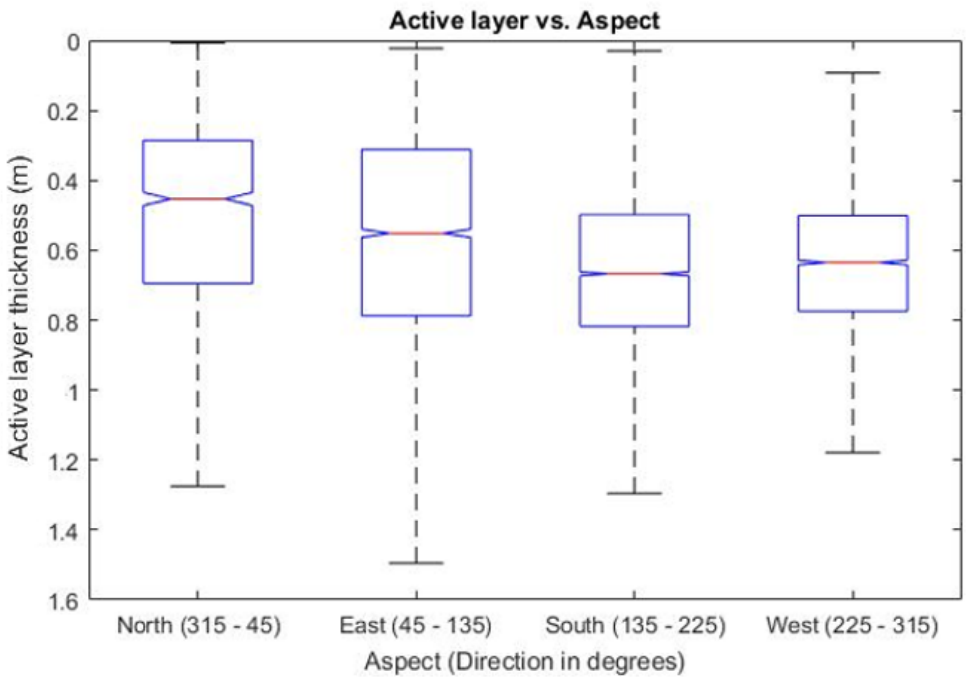

Figure 14*: Estimated ALT vs. Aspect for the major four direction. Class median (red line), 25 & 75 percentile (blue box), minimum & maximum (whiskers).*

When comparing the ES-ALT between depressions, flat terrain (slope < 2°) and sloped terrain (slope >2°), the classes differ significantly (Kruskal-Wallis test, p-value ~ 0). Depressions have the lowest mean ES-ALT with 0.54 m, whilst flat and sloped terrain have larger ES-ALT. The difference between sloped and flat terrain is also significant (Wilcoxon rank sum test, p-value ~ 0) with flat terrain having the largest mean ES-ALT of 0.68 m (Fig. 15).

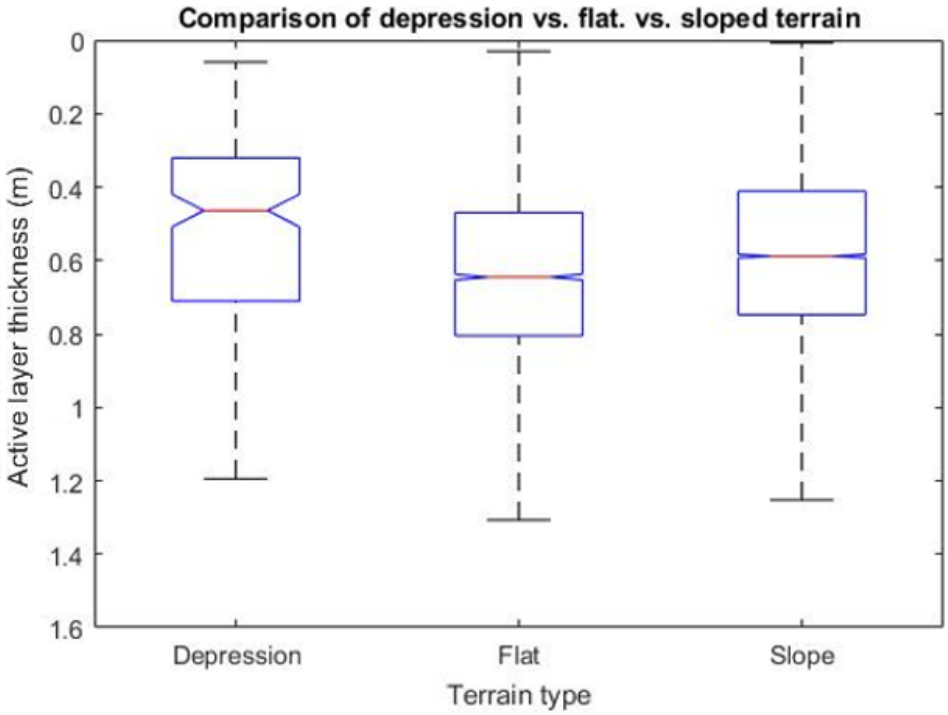

Figure 15*: Terrain comparison with classes depression, flat and slope. Class median (red line), 25 & 75 percentile (blue box), minimum & maximum (whiskers).*

The ALT differs significantly (Wilcoxon rank sum test: p-value ~ 0) between vegetated and non-vegetated areas (Table A3, Fig. A5) with vegetated areas having a deeper mean ES-ALT (0.66 m vs. 0.55 m). However, the on average smaller ES-ALT in non-vegetated areas is characterized by a larger variability (Fig. 16).

Also, the individual vegetation classes are statistically different (Kruskal-Wallis test: p-value ~ 0) (Fig. 16). Both the vegetation classes adapted to the wettest (Fen) and driest (Dryas & Cassiope) conditions show the smallest ES-ALT and are statistically similar based on Wilcoxon rank sum tests (p-value = 0.78 for Fen & Dryas, p-value = 0.25 for Fen & Cassiope). This opposes the hypothesized smaller ES-ALT in Fen areas (hypothesis 4). Nevertheless, the lowest mean ES-ALT is located beneath Fen areas with 0.62 m and the largest ES-ALT is located beneath Salix vegetation with a mean of 0.72 m (Fig. 16).

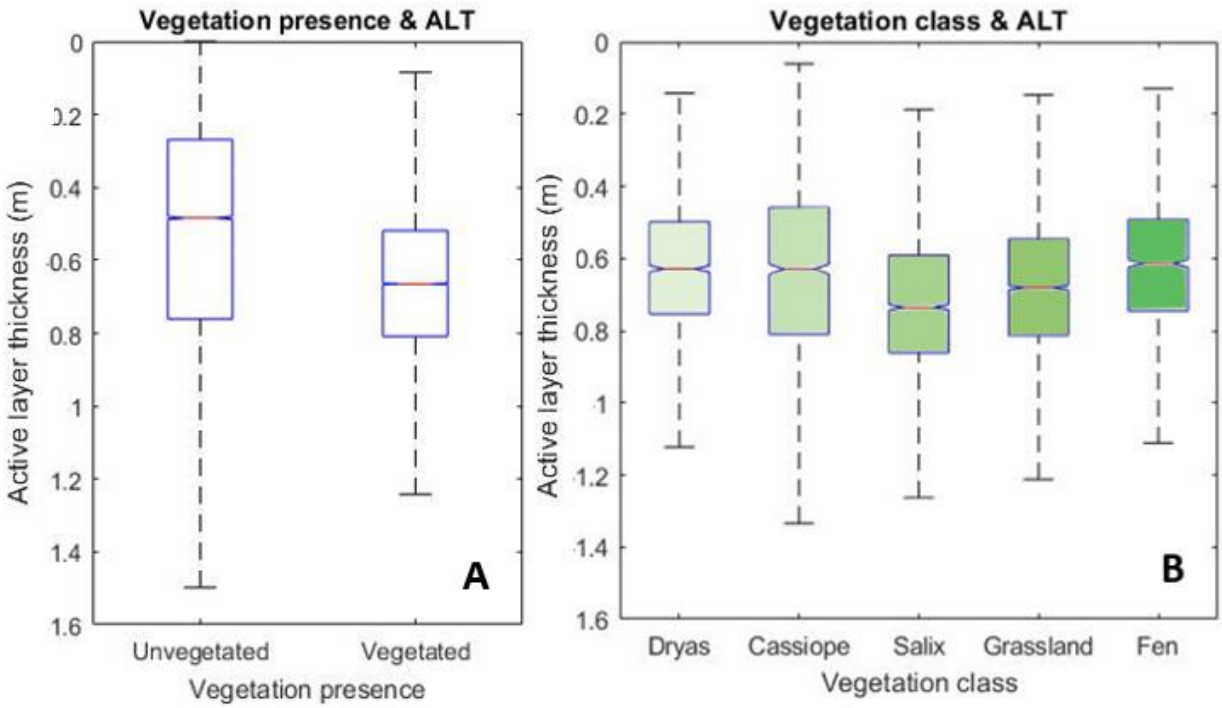

***Figure 16**: **A** = Estimated ALT vs. Vegetation presence, **B** = Estimated ALT vs. Vegetation classes with background box colour indicating soil water content (light = driest, dark = wettest). Box plots show median (red line), 25 & 75 percentile (blue box), minimum & maximum (whiskers).*

5 Discussion

5.1 Ability of method to estimate ALT

The results of this study showed that the remotely sensed estimated ALT (ES-ALT) aligned well to the in situ measured ALT (M-ALT), with both the temporal development and the maximum of the ES-ALT being statistically similar to the M-ALT. However, one outlier was observed, with the ALT being strongly underestimated at the Runway station.

The subsidence was larger in water saturated areas, where higher ice content in the upper soil layers induces a stronger volume change compared to areas with lower ice content. This supports hypothesis 2. The finding aligns with other studies, which had related water content field measurements to subsidence measurements. Chen et al. (2020) compared field measurements of soil water content to DInSAR subsidence measurements and found a significant positive relationship between ice content and subsidence. Also, Daout et al. (2017) found the ground oscillations caused by the freeze-thaw cycle to be smaller in drier soils.

Even though the ES-ALT is, as hypothesized (1), statistically similar to the M-ALT, the evaluation of the ES-ALT is dominated by one outlier: the field measurements at the Runway station were underestimated strongly. Several factors could have caused this difference. Firstly, an imprecise location of the point might have caused this difference, as only 40 m north of the Runway station, an ALT of 1.5 m was estimated, which aligns with the M-ALT. Secondly, the soil moisture content might have been overestimated due to the deep AL just north of this point. If the sloped permafrost table caused water to flow northwards, the assumption of saturated conditions in the lower part of the soil column might have caused an error. The difference might have also been generated by the method underestimating enhanced thaw known to occur beneath thicker snow cover due to less winter cooling. The location is known to hold snow longer and as snow insulates the soil from winter cool down, faster thaw progression has been observed beneath thicker snow cover (Nowinski et al. 2010; Johansson et al. 2013). Yet, other studies observed decreased ALT due to the delayed thaw (Seppala 2003; Hinkel and Hurd 2006), which would not explain the outlier. Lastly, the field measurements at the Runway station might have been biased by water percolating down along the borehole of the thermistor string. This could have caused deeper recordings of the ALT than actually exists in the surrounding soil (Christiansen et al. 2008).

The evaluation of the relationship between absolute ES-ALT difference to M-ALT at each station vs. the respective saturation fraction showed a significant trend towards a larger error in areas with a lower saturation fraction. This supports hypothesis 5. As none of the field measurement points is located solely in a dry vegetation type (Dryas or Cassiope) the significance of the error in drier areas could be larger or smaller than measured with the current error analysis. The analysis of the ALT regarding vegetation classes did show discrepancies for the drier vegetation classes Dryas and Cassiope. Based on Elberling et al. (2008) the drier vegetation types Dryas and Cassiope should have the largest ALT, followed in decreasing ALT by Salix, Grassland and Fen (wettest vegetation type). Thus, the saturation fraction and thereby vegetation type should be negatively correlated to ALT (Elberling et al. 2008). The expected distribution was not visible in the ES-ALT, which points also towards a less accurate ES-ALT in areas with drier soils. This is supported by Liu et al. (2012), who predicted that the sensitivity of the estimated result to the saturation fraction increases with drier soil conditions.

The ES-ALT distribution of Salix, Grassland and Fen aligns better with findings from Elberling et al. (2008). The overall ES-ALT is larger than that recorded for the vegetation types in 2005 (Elberling et al. 2008). Considering the increase in ALT between 2005 and 2017 the ES-ALT appears more reasonable in these vegetation classes (Elberling et al. 2013; Strand et al. 2020).

Fen areas were, as hypothesized (4), characterized by shallow ES-ALT, which can be explained both by the existing peat layer (Elberling et al. 2008) and the related high porosity and thereby ice content of the soil. ALT has a strong negative correlation to peat thickness because of the low thermal conductivity of peat as well as the large amount of energy needed to melt the ice in the very porous peat layer. It has been approximated that peat requires roughly 1.5 times the energy needed for mineral soils to thaw to a similar soil depth (Atchley et al. 2016).

The ES-ALT was larger in vegetated areas than in non-vegetated areas, yet the ES-ALT varied more in non-vegetated areas. This variability might reflect the diverse conditions from abrasion plateaus to areas dominated by boulders. In general, these non-vegetated areas with mineral soil should have a deeper active layer, as mineral soil has a higher thermal conductivity and a lower porosity (Nelson 1997; Atchley et al. 2016). Exposed rock has a high thermal conductivity and therefore should cause relatively large ALT (Elberling et al. 2008). It is likely that the large amount of boulders in the non-vegetated areas decreased the signal of the thaw subsidence and that the ALT is therefore underestimated in these areas.

The insignificant relationship of the ES-ALT to stream vicinity shows how complex ALT dynamics are, as it can be assumed that the insignificant result is caused by interference of other factors like the soil structure or topography the further away the closest stream is. Rivers have been found on regional scale to be positively correlated to ALT (Nelson 1997) and riverbeds are overall deeper thawed (thaw bulb), due to the heat transport of the water discharge (Hinkel 2003; Brosten et al. 2009). Yet, the extent of the thaw bulb is limited to the extent of the riverbed and could therefore have been interfered by other factors.

Southern aspects were, as hypothesized (3), characterized by the deepest ES-ALT, resulting from the larger amount of incoming solar radiation received by the ground surface (Zhao et al. 2000). This not only affects the thaw process itself, but also causes earlier snow melt and therefore an earlier thawing onset of the AL. Thus, deeper ALT on southern slopes has been found at many sites (Nelson 1997; Gao et al. 2016; Cao et al. 2017) and the aspect is often incorporated when modelling the ALT distribution (Christiansen et al. 2008; Li et al. 2017).

Depressions showed a significantly lower ES-ALT than sloped or flat areas, which could be related to prolonged snow cover (Christiansen et al. 2008) as well as high soil moisture content and ground ice (Gao et al. 2018), requiring more energy for thawing. This result aligns with field measurements from Gao et al. (2016). However, soil moisture in depressions can also cause deeper ALT, if the high thermal conductivity of water outweighs the energy needed to melt the large amount of ground ice (Nelson 1997; Wright et al. 2009; Guan et al. 2010; Gangodagamage et al. 2014). The largest ALT in flat terrain could be related to less ice content in the AL and an earlier thaw onset caused by shallower snow depths due to wind exposure (Woo 2012). The intermediate ALT on slopes could be the result of a combination of the different aspect angles and enhanced thawing due to the heat contribution of snow-meltwater runoff from higher elevations (Atchley et al. 2016; Gao et al. 2016).

Overall, both the comparison to field measurements and to the environmental parameters indicated a good performance of the method, especially in areas with a high saturation. The hypothesized larger subsidence in water-saturated areas was reflected in the subsidence result and the ES-ALT was larger on south-facing slopes and lower in peat-rich Fens. Nevertheless,

the results of the environmental parameter evaluation are characterized by high variability, which highlights complex interactions of the different factors contributing to the spatial ALT distribution. The larger difference to the in-situ ALT with decreasing saturation of the soil indicates the demand for further improvements of the ALT estimate. This could be accomplished by collecting soil moisture field data of the year previous to the subsidence analysis to receive a more accurate NSMI-soil moisture relationship, as well as by including a more detailed modelling of the saturation in the lower AL.

5.2 Sources of error in study

The evaluation based on the field measurements is limited by the amount and distribution of the field sites within the study area. The sample size of 9 sites is statistically not sufficient to draw robust conclusions. Also, the field measurements are unequally distributed regarding vegetation types and represent mostly Fen (n = 3), Salix (n = 3), Grassland (n = 1), Cassiope (n = 1) and Barrens (n = 1). Therefore, it is more uncertain how the ALT estimate performs in drier vegetation sites, as there is less data available for the dry vegetation sites (n = 2).

The ALT estimate of this study is limited by the quality of the saturation fraction and porosity data, as well as the uncertainty of the subsidence observations.

It is difficult to evaluate the subsidence observations because no field measurements on the seasonal subsidence exist for the study area. The observed seasonal subsidence ranges within a reasonable interval compared to other studies (Liu et al. 2012; Wang et al. 2018). However, as the relative subsidence has to be calibrated with a stable point in the area, it is likely that an error was introduced by the choice of the calibration point. The approach of using a point with very high coherence (e.g. no change between image pairs) has been previously applied (Liu et al. 2012), but the two 12-day intervals with no subsidence indicate that the calibration point was not always sufficient. This could be a result of the calibration point not being completely stable (coherence = 0.93 and not 1).

Additionally, the subsidence could have been affected by the quality of the used DEM for the DInSAR processing. With the high spatial resolution (5 m) and an accuracy of 3-5 m the DEM was still more precise than other global DEM sources (NERI 2000; EEA 2017), yet the accuracy could have affected the DInSAR phase difference retrieval (Yu et al. 2007).

The subsidence result could also have been biased by assuming no horizontal movement. This condition is required to transfer the Line-of-Sight displacement into vertical displacement using trigonometric functions (Fuhrmann and Garthwaite 2019). The upper slopes in Zackenberg valley experience creep displacement and small solifluction sites can also be found in the lower valley, with movement rates at one site averaging 1.25 cm / year (Christiansen et al. 2008). It is therefore unsure if creep movement might have also affected the subsidence results in the lower valley.

Another possible error source is the saturation fraction estimate, as only limited field data was available. The ice content in the thawing soil is dependent on the saturation of the soil at the end of the previous thawing season (e.g. 2016). To incorporate the spatial variability, the NSMI from mid-August 2016 was compared to the existing soil moisture dataset. However, these soil moisture measurements were from July in a different year with similar climatic conditions (Fig. A7). It is still assumed that the relative distribution in the upper soil layer is correct, yet it is uncertain how precise the saturation depth estimation was. In addition, the ice content could

have been increased during the spring warming stage by percolation and refreezing of snow melt water into unsaturated soil pores of the AL (Scherler et al. 2010).

The porosity estimate used in this study could have been affected by using the average organic matter measurements based on 9 geomorphological classes. As the peat thickness is strongly influencing the ALT this could have further caused imprecise results (Atchley et al. 2016).

Lastly, the evaluation could have been affected by the quality of the field measurements. The manual probing measurements can include a human bias, but more importantly it is questionable how reliable the thermistor measurements are. The thermistor string installation could alter the surrounding ALT by enabling percolation of water along the tube. The heat capacity of the water could enhance the thawing and thereby the ALT could be overestimated at thermistor sites (Christiansen et al. 2008).

A limitation for the robustness of the statistical test results in this study is existing spatial autocorrelation. This tendency of areas close together having similar values is of importance, as it can bias the statistical data evaluation (Dale and Fortin 2014). When testing the ALT across the study area for spatial autocorrelation with the Global Moran's I statistic the null hypothesis of spatial randomness had to be rejected (p-value ~ 0). The Moran's Index of 0.88 and positive z-score (695) indicates that the ALT result is more spatially clustered than if no spatial autocorrelation would exist. This proves that the estimated ALT is not randomly distributed. However, the spatial autocorrelation increases the likelihood of wrongly rejecting the null hypothesis in statistical tests (Type 1 error), which should be considered when evaluating the robustness of the statistical tests performed in this study (Dale and Fortin 2014).

5.3 Overall method evaluation and comparison

5.3.1 Limitations of method

The method is generally limited by the accuracy and spatial resolution of the input data.

Soil moisture varies significantly throughout the seasons and thus the time of the estimation is critical. Further, the large soil moisture variations within very short spatial distances in permafrost areas requires high resolution data (Hinkel 2003). The saturation fraction might be derived for the topsoil through remote sensing, but the approach in this study using the NSMI only showed an intermediate coefficient of determination (r^2) of 0.64 between the satellite index and the calibration measurements. It is additionally uncertain how precise the subsurface saturation fraction estimates are, which highlights that the precision of the method decreases, if the soil conditions are not uniformly saturated.

To improve the saturation fraction estimate, it might be possible to incorporate ground water models, also to address permafrost table depth variations (Wang et al. 2018). Further, new surface soil moisture estimates using SAR-imagery have shown to deliver soil moisture estimates for the topsoil at high spatial resolution. However, also these products require calibration and are limited by interference of other factors on the signal returning to the satellite sensor (Kornelsen and Coulibaly 2013). Other current remotely sensed soil moisture products like SMAP combine SAR with passive microwave radiometer measurements and aim for high accuracies. Yet, they are limited in resolution (currently 9 km above 60° latitude for SMAP) (Entekhabi 2014; O'Neill 2020) and can therefore be expected to lead to inaccurate results, considering the high spatial variability of the ALT.

The estimation of the porosity is dependent on accurate soil texture and especially organic matter estimates. Datasets on soil carbon density, soil texture and other soil parameters exist (e.g. SoilGrids used for this study). Yet, they are based on upscaling methods of soil profile observations and thus limited in their accuracy (30 – 70 % data accuracy for SoilGrids products) (ISRIC 2020a).

The subsidence estimate is limited by the DEM used for the DInSAR processing. High spatial resolution as well as accuracy of the DEM are of large benefit for precise retrievals of the phase difference and thereby the ground displacement (Yu et al. 2007; Walter and Bush 2012).

Further, the sensitivity of the DInSAR subsidence estimate to horizontal displacement restricts the application of the DInSAR approach used in this study. If horizontal displacement exists more complex analysis is required in order to derive the vertical component of the derived surface displacement (Fuhrmann and Garthwaite 2019). As solifluction is common in permafrost regions and is predicted to increase with AL deepening, this limits the application of the DInSAR approach used in this study to flat areas (Akerman 2005; Mithan 2018).

The method is also constrained to applications within the snow-free part of the thawing season, as the subsidence measurement is more prone to errors (coherence loss) if snow or oversaturated soil covers a large part of the study area (Liu et al. 2010). If field measurements are available, these can be used as an indicator of the thawing start, yet without these it is difficult to derive the maximum active layer thickness.

Of these limitations, the method can be expected to be most sensitive to the subsidence observations if the ALT is estimated for saturated conditions (Lui et al. 2012).

Yet, with decreasing soil saturation the impact of the correct saturation fraction increases in importance. Changes in porosity have less of an impact. This is supported by accuracy evaluations of Liu et al. (2012) and can also be seen when evaluating the sensitivity of the ALT estimate formula (Equation 3) to varying subsidence, porosity or saturation fractions, whilst the remaining values remain constant (Fig. 17). The sensitivity to the subsidence is linear, yet the saturation fraction affects the estimate in a logarithmic manner. Until roughly 60 % saturation the saturation fraction acts nearly linearly, yet below this value the exact saturation becomes of larger importance, as inaccuracies have a higher impact on the ALT estimate (notice also scale of ALT from 0 – 12 m). Therefore, the ALT estimate is especially sensitive to the correct saturation fraction in drier areas, where small difference in the saturation fraction can cause large differences in the ALT estimate (Fig. 17). Porosity affects the ALT estimate to a smaller extent compared to the saturation fraction.

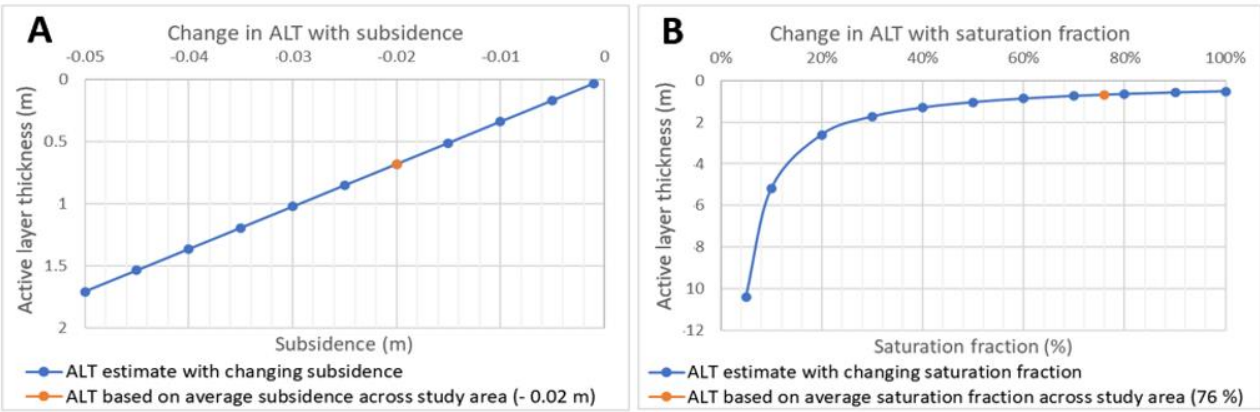

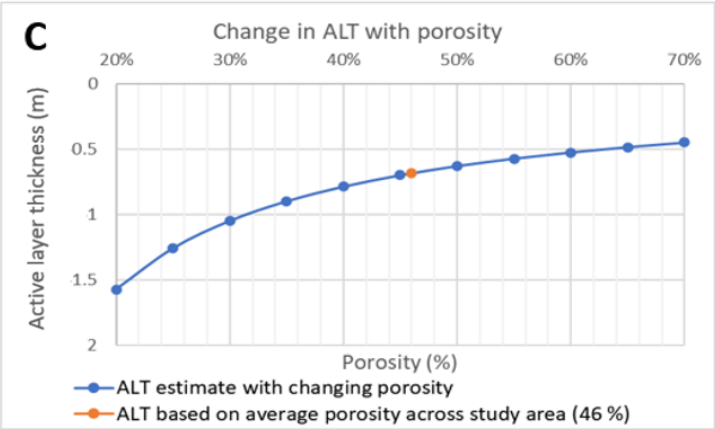

Figure 17: *Sensitivity of ALT estimate to subsidence (**A**), saturation fraction (**B**) and porosity (**C**) values, if the other parameters are constant (subsidence = -0.02 m, porosity = 46 %, saturation. fraction = 76 %). Values of other parameters are based on mean result across study site.*

5.3.2 Comparison to other methods

The two main other methods to derive ALT distribution are interpolation of field measurements and modelling.

Interpolation of field measurements only allows reliable results if measurements are available at a very high spatial resolution (Hinkel 2003), which makes this method unsuitable for monitoring of ALT at a larger scale.

For the modelling of the ALT different approaches exist. Most commonly they built up on the Stefan model, which relates the thawing to the accumulated ground surface degree-day total (Riseborough 2008). As the active layer is affected by a variety of factors which also interact with each other, ALT models are limited by the processes and factors explicitly considered in the model (e.g. heat transfer in soil, soil structure, vegetation, snow cover). Due to the scarcity of field measurements and the coarse spatial resolution of input data available for modelling (e.g. climate raster data like surface and air temperature, vegetation cover), it is difficult to precisely represent the high ALT variability know to occur at local scales (Streletskiy et al. 2012).

The estimation of the ALT through combining subsidence with porosity and saturation fraction has the advantage that the method does not require the modelling of the complex interplay of all the factors affecting the AL. The subsidence accounts for differences in insolation, topography and soil conditions as well as snow distribution. However, the determination of the ice content is critical, and the processing of the subsidence is sensitive to errors based on insufficient ground calibration and errors in retrieving the phase difference.

Based on these characteristics of the different methods, field measurements can be seen as most appropriate for small-scale high resolution ALT inventories, whilst modelling is very useful for large-scale investigations with a lower spatial resolution. The ground subsidence method is suited for intermediate-scale mapping and to upscale field measurements to ALT estimates on km-scales.

6 Conclusion

This thesis work aimed at evaluating the possibility to relate ground subsidence as estimated by the DInSAR method to seasonal ALT progression by considering the volume change induced by the phase transition from ice to water of the water content in the soil.

The ground subsidence method performed overall well in estimating both the maximum ALT and the ALT development in the study region around Zackenberg, NE Greenland for 2017. The estimate across the valley is within the range of values found at the field measurement sites and both the development throughout the thawing season and the maximum ALT are statistically similar to the measurements.

The hypothesized larger subsidence in water-saturated areas was reflected in the subsidence result and the estimated ALT follows a distribution which is plausible based on other environmental factors: larger ALT was found on south facing slopes and lower ALT in depressions and peat-rich vegetation systems.

Yet, the overall accuracy of the estimated ALT is uncertain, as limited field measurements were available, especially from dry vegetation types and non-vegetated areas, for which the estimated ALT is likely too low. This was indicated by a significantly larger difference to the in-situ data at measurement stations with drier soil as well as a lower than expected ALT under dry vegetation types based on other studies. It points out the difficulties of applying the method in an area which is very heterogenous in soil porosity as well as soil saturation fraction.

The method is promising to resolve ALT distribution with high spatial resolution (20 m in this study). However, the result is strongly dependent on correct subsidence observations as well as accurate estimations of the saturation fraction and porosity to derive the ice content. For drier soils, the sensitivity of the method to the correct saturation fraction estimate is increased. The method is further limited to snow-free conditions and due to the large spatial variability of the ALT, input data of high spatial resolution is required.

As found in other studies, the method can be applied for ALT monitoring at water-saturated sites. It is however recommended to adapt the subsidence processing so that 3D-displacement is considered. For non-saturated areas, it is suggested that future studies incorporate modelling of the soil ice content, which could possibly be combined with topsoil saturation estimates based on the Normalised Soil Moisture Index. Further evaluation with more extensive field measurement points and over multiple sites and years is needed to evaluate the application of the method at sites with non-saturated soil conditions.

7 References

Abe, T., G. Iwahana, P. V. Efremov, A. R. Desyatkin, T. Kawamura, A. Fedorov, Y. Zhegusov, K. Yanagiya, et al. 2020. Surface displacement revealed by L-band InSAR analysis in the Mayya area, Central Yakutia, underlain by continuous permafrost. *Earth, Planets and Space,* 72. DOI: 10.1186/s40623-020-01266-3

Akerman, H. J. 2005. Relations between slow slope processes and active-layer thickness 1972–2002, Kapp Linné, Svalbard. *Norsk Geografisk Tidsskrift - Norwegian Journal of Geography,* 59**:** 116-128. DOI: 10.1080/00291950510038386

Atchley, A. L., E. T. Coon, S. L. Painter, D. R. Harp, and C. J. Wilson. 2016. Influences and interactions of inundation, peat, and snow on active layer thickness. *Geophysical Research Letters,* 43**:** 5116-5123. DOI: 10.1002/2016gl068550

Beven, K. J., and M. J. Kirkby. 1979. A physically based, variable contributing area model of basin hydrology / Un modèle à base physique de zone d'appel variable de l'hydrologie du bassin versant. *Hydrological Sciences Bulletin,* 24**:** 43-69. DOI: 10.1080/02626667909491834

Biskaborn, B. K., S. L. Smith, J. Noetzli, H. Matthes, G. Vieira, D. A. Streletskiy, P. Schoeneich, V. E. Romanovsky, et al. 2019. Permafrost is warming at a global scale. *Nature Communications,* 10. DOI: ARTN 26410.1038/s41467-018-08240-4

Boike, J., K. Roth, and P. P. Overduin. 1998. Thermal and hydrologic dynamics of the active layer at a continuous permafrost site (Taymyr Peninsula, Siberia). *Water Resources Research,* 34**:** 355-363. DOI: 10.1029/97wr03498

Braun, A., and L. Veci. 2020. TOPS Interferometry Tutorial. European Space Agency.

Brosten, T. R., J. H. Bradford, J. P. Mcnamara, M. N. Gooseff, J. P. Zarnetske, W. B. Bowden, and M. E. Johnston. 2009. Estimating 3D variation in active-layer thickness beneath arctic streams using ground-penetrating radar. *Journal of Hydrology,* 373**:** 479-486. DOI: 10.1016/j.jhydrol.2009.05.011

Brown, J., K. M. Hinkel, and F. E. Nelson. 2000. The circumpolar active layer monitoring (CALM) program: Research designs and initial results. *Polar Geography,* 24**:** 166-258. DOI: 10.1080/10889370009377698

Brown, J. F., O. ;Heginbottom, J. A. ; Melnikov, E. . 2002. Circum-Arctic Map of Permafrost and Ground-Ice Conditions Boulder, Colorado USA: NSIDC: National Snow and Ice Data Center.

Cable, S., H. H. Christiansen, A. Westergaard-Nielsen, A. Kroon, and B. Elberling. 2018. Geomorphological and cryostratigraphical analyses of the Zackenberg Valley, NE Greenland and significance of Holocene alluvial fans. *Geomorphology,* 303**:** 504-523. DOI: 10.1016/j.geomorph.2017.11.003

Cao, B., S. Gruber, T. Zhang, L. Li, X. Peng, K. Wang, L. Zheng, W. Shao, and H. Guo. 2017. Spatial variability of active layer thickness detected by ground-penetrating radar in the Qilian Mountains, Western China. *Journal of Geophysical Research: Earth Surface,* 122**:** 574-591. DOI: 10.1002/2016jf004018

CEN. 2020. ADAPT Permafrost Research Progam - Communications. Retrieved 30 December, 2020, from http://www.cen.ulaval.ca/adapt/communications/permafrost101.php

Chen, C. W., and H. A. Zebker. 2002. Phase unwrapping for large SAR interferograms: statistical segmentation and generalized network models. *IEEE Transactions on Geoscience and Remote Sensing,* 40**:** 1709-1719. DOI: 10.1109/tgrs.2002.802453

Chen, J., Y. Wu, M. O'Connor, M. B. Cardenas, K. Schaefer, R. Michaelides, and G. Kling. 2020. Active layer freeze-thaw and water storage dynamics in permafrost environments inferred from InSAR. *Remote Sensing of Environment,* 248**:** 112007. DOI: 10.1016/j.rse.2020.112007

Christiansen, H. H., C. Sigsgaard, O. Humlum, M. Rasch, and B. U. Hansen. 2008. Permafrost and Periglacial Geomorphology at Zackenberg. In *High-Arctic Ecosystem Dynamics in a Changing Climate,* 151-174. Amsterdam: Elsevier.

Cosby, B. J., G. M. Hornberger, R. B. Clapp, and T. R. Ginn. 1984. A Statistical Exploration of the Relationships of Soil Moisture Characteristics to the Physical Properties of Soils. *Water Resources Research,* 20**:** 682-690. DOI: 10.1029/wr020i006p00682

Dale, M. R. T. and M.-J. Fortin. 2014. Spatial autocorrelation and inferential tests. In *Spatial Analysis - A Guide For Ecologists*. Cambridge: Cambridge University Press.

Daout, S., M. P. Doin, G. Peltzer, A. Socquet, and C. Lasserre. 2017. Large-scale InSAR monitoring of permafrost freeze thaw cycles on the Tibetan Plateau. *Geophysical Research Letters,* 44**:** 901-909. DOI: 10.1002/2016gl070781

EEA. 2017. Overview of Global DEMs. e-GEOS and GAF AG. Report.

Elberling, B., M. P. Tamstorf, A. Michelsen, M. F. Arndal, C. Sigsgaard, L. Illeris, C. Bay, B. U. Hansen, et al. 2008. Soil and Plant Community-Characteristics and Dynamics at Zackenberg. In *High-Arctic Ecosystem Dynamics in a Changing Climate*, 223-248. Amsterdam: Elsevier.

Elberling, B., A. Michelsen, C. Schädel, E. A. G. Schuur, H. H. Christiansen, L. Berg, M. P. Tamstorf, and C. Sigsgaard. 2013. Long-term CO2 production following permafrost thaw. *Nature Climate Change*, 3: 890-894. DOI: 10.1038/nclimate1955

Entekhabi, D., S. Yueh, P. O'Neill, K. Kellogg et al. 2014. SMAP Handbook - Soil Moisture. Active Passive Jet Propulsion Laboratory, Report, Pasadena, California, 182 pp.

ESA. 2020a. SAR Instrument. Retrieved 15. December, 2020, from https://sentinel.esa.int/web/sentinel/technical-guides/sentinel-1-sar/sar-instrument.

ESA. 2020b. Copernicus Open Access Hub. Retrieved 15. December, 2020, from https://scihub.copernicus.eu/.

Frauenfeld, O. W. 2004. Interdecadal changes in seasonal freeze and thaw depths in Russia. *Journal of Geophysical Research*, 109. DOI: 10.1029/2003jd004245

Fuhrmann, T., and M. C. Garthwaite. 2019. Resolving Three-Dimensional Surface Motion with InSAR: Constraints from Multi-Geometry Data Fusion. *Remote Sensing*, 11. DOI: 10.3390/rs11030241

Gangodagamage, C., J. C. Rowland, S. S. Hubbard, S. P. Brumby, A. K. Liljedahl, H. Wainwright, C. J. Wilson, G. L. Altmann, et al. 2014. Extrapolating active layer thickness measurements across Arctic polygonal terrain using LiDAR and NDVI data sets. *Water Resources Research*, 50**:** 6339-6357. DOI: 10.1002/2013wr014283

Gao, B.-C. 1996. NDWI—A normalized difference water index for remote sensing of vegetation liquid water from space. *Remote Sensing of Environment*, 58**:** 257-266. DOI: 10.1016/s0034-4257(96)00067-3

Gao, T., T. Zhang, X. Wan, S. Kang, M. Sillanpää, Y. Zheng, and L. Cao. 2016. Influence of microtopography on active layer thaw depths in Qilian Mountain, northeastern Tibetan Plateau. *Environmental Earth Sciences*, 75. DOI: 10.1007/s12665-015-5196-7

Gao, T., T. Zhang, H. Guo, Y. Hu, J. Shang, and Y. Zhang. 2018. Impacts of the active layer on runoff in an upland permafrost basin, northern Tibetan Plateau. *PLOS ONE*, 13: e0192591. DOI: 10.1371/journal.pone.0192591

GEM. 2000. High resolution digital terrain model. Retrieved 15. December, 2020, from https://g-e-m.dk/gem-localities/zackenberg/maps/high-resolution/

GEM. 2020a. Greenlandic Ecosystem Monitoring Database. Retrieved 15. December, 2020, from https://data.g-e-m.dk/

GEM. 2020b. Maps. Retrived 15. December, 2020, from https://g-e-m.dk/gem-localities/zackenberg/maps/

Gruber, S. 2012. Derivation and analysis of a high-resolution estimate of global permafrost zonation. *The Cryosphere*, 6**:** 221-233. DOI: 10.5194/tc-6-221-2012

Guan, X. J., C. J. Westbrook, and C. Spence. 2010. Shallow soil moisture – ground thaw interactions and controls – Part 1: Spatiotemporal patterns and correlations over a subarctic landscape. *Hydrology and Earth System Sciences*, 14**:** 1375-1386. DOI: 10.5194/hess-14-1375-2010

Hansen, B. U., C. Sigsgaard, L. Rasmussen, J. Cappelen, J. Hinkler, S. H. Mernild, D. Petersen, M. P. Tamstorf, M. Rasch, and B. Hasholt. 2008. Present-Day Climate at Zackenberg. In *High-Arctic Ecosystem Dynamics in a Changing Climate*, 111-149. Amsterdam: Elsevier.

Harris, C. 2005. Climate Change, Mountain Permafrost Degradation and Geotechnical Hazard. In *Global Change and Mountain Regions. Advances in Global Change Research*, ed. U. M. B. Huber, H.K.M. Bugmann, M.A. Reasoner. 215-224. Dordrecht: Springer.

Haubrock, S. N., S. Chabrillat, C. Lemmnitz, and H. Kaufmann. 2008. Surface soil moisture quantification models from reflectance data under field conditions. *International Journal of Remote Sensing*, 29**:** 3-29. DOI: 10.1080/01431160701294695

Hinkel, K. M. 2003. Spatial and temporal patterns of active layer thickness at Circumpolar Active Layer Monitoring (CALM) sites in northern Alaska, 1995–2000. *Journal of Geophysical Research*, 108. DOI: 10.1029/2001jd000927

Hinkel, K. M., and J. K. Hurd. 2006. Permafrost destabilization and thermokarst following snow fence installation, Barrow, Alaska, USA. *Arctic Antarctic and Alpine Research*, 38**:** 530-539. DOI: 10.1657/1523-0430(2006)38[530:Pdatfs]2.0.Co;2

Hollesen, J., B. Elberling, and P. E. Jansson. 2011. Future active layer dynamics and carbon dioxide production from thawing permafrost layers in Northeast Greenland. *Global Change Biology*, 17**:** 911-926. DOI: 10.1111/j.1365-2486.2010.02256.x

Hong, E., R. Perkins, and S. Trainor. 2014. Thaw Settlement Hazard of Permafrost Related to Climate Warming in Alaska. *Arctic*, 67**:** 93-103.

Hugelius, G., J. G. Bockheim, P. Camill, B. Elberling, G. Grosse, J. W. Harden, K. Johnson, T. Jorgenson, et al. 2013. A new data set for estimating organic carbon storage to 3 m depth in soils of the northern circumpolar permafrost region. *Earth System Science Data*, 5**:** 393-402. DOI: 10.5194/essd-5-393-2013

Hugelius, G., J. Strauss, S. Zubrzycki, J. W. Harden, E. A. G. Schuur, C.-L. Ping, L. Schirrmeister, G. Grosse, et al. 2014. Estimated stocks of circumpolar permafrost carbon with quantified uncertainty ranges and identified data gaps. *Biogeosciences*, 11**:** 6573-6593. DOI: 10.5194/bg-11-6573-2014

ISRIC. 2020a. FAQ SoilGrids. Retrieved 15. December, 2020, from https://www.isric.org/explore/soilgrids/faq-soilgrids.
ISRIC. 2020b. SoilGrids. Retrieved 15. December, 2020, from https://soilgrids.org/.
Jaya, L. M. G., J. Safani, A. Okto, M. Hasbi, and A. Kadir. 2020. Ground deformation analysis on road infrastructure in north buton Indonesia using interferometric synthetic aperture radar (Insar). *IOP Conference Series: Earth and Environmental Science,* 419**:** 012095. DOI: 10.1088/1755-1315/419/1/012095
Jia, Y., J.-W. Kim, C.K. Shum, Z. Lu, X. Ding, L. Zhang, K. Erkan, C.-Y. Kuo, et al. 2017. Characterization of Active Layer Thickening Rate over the Northern Qinghai-Tibetan Plateau Permafrost Region Using ALOS Interferometric Synthetic Aperture Radar Data, 2007–2009. *Remote Sensing,* 9**:** 84. DOI: 10.3390/rs9010084
Johansson, M., T. V. Callaghan, J. Bosio, H. J. Akerman, M. Jackowicz-Korczynski, and T. R. Christensen. 2013. Rapid responses of permafrost and vegetation to experimentally increased snow cover in sub-arctic Sweden. *Environmental Research Letters,* 8. DOI: 10.1088/1748-9326/8/3/035025
Jorgenson, M. T., V. Romanovsky, J. Harden, Y. Shur, J. O'Donnell, E. A. G. Schuur, M. Kanevskiy, and S. Marchenko. 2010. Resilience and vulnerability of permafrost to climate change. *Canadian Journal of Forest Research,* 40**:** 1219-1236. DOI: 10.1139/x10-060
Kanji, G. K. 2006. 100 Statistical tests. London, Thousand Oaks, New Delhi: SAGE Publications.
Kornelsen, K. C., and P. Coulibaly. 2013. Advances in soil moisture retrieval from synthetic aperture radar and hydrological applications. *Journal of Hydrology,* 476**:** 460-489. DOI: 10.1016/j.jhydrol.2012.10.044
Lantz, B. 2013. The large sample size fallacy. *Scandinavian Journal of Caring Sciences,* 27**:** 487-492. DOI: 10.1111/j.1471-6712.2012.01052.x
Li, A., X. Tan, W. Wu, H. Liu, and J. Zhu. 2017. Predicting active-layer soil thickness using topographic variables at a small watershed scale. *PLOS ONE,* 12**:** e0183742. DOI: 10.1371/journal.pone.0183742
Li, Z., R. Zhao, J. Hu, L. Wen, G. Feng, Z. Zhang, and Q. Wang. 2015. InSAR analysis of surface deformation over permafrost to estimate active layer thickness based on one-dimensional heat transfer model of soils. *Scientific Reports,* 5**:** 15542. DOI: 10.1038/srep15542
Liu, L., T. Zhang, and J. Wahr. 2010. InSAR measurements of surface deformation over permafrost on the North Slope of Alaska. Journal of Geophysical Research, 115. DOI: 10.1029/2009jf001547
Liu, L., K. Schaefer, T. Zhang, and J. Wahr. 2012. Estimating 1992-2000 average active layer thickness on the Alaskan North Slope from remotely sensed surface subsidence. *Journal of Geophysical Research: Earth Surface,* 117**:** F01005. DOI: 10.1029/2011jf002041
Mithan, H. T. 2018. Quantifying the dynamic response of permafrost and slope stability to a changing climate. PhD Thesis. Cardiff, UK: Cardiff University.
Moran, P. A. P. 1950. Notes on Continuous Stochastic Phenomena. *Biometrika,* 37**:** 17-23. DOI: 10.2307/2332142.
Moreira, A., P. Prats-Iraola, M. Younis, G. Krieger, I. Hajnsek, and K.P. Papathanassiou. 2013. A Tutorial on Synthetic Aperture Radar. *IEEE Geoscience and Remote Sensing Magazine,* 1**:** 6 - 43. DOI: 10.1109/MGRS.2013.2248301
Morel, X., B. Decharme, C. Delire, G. Krinner, M. Lund, B. U. Hansen, and M. Mastepanov. 2019. A New Process-Based Soil Methane Scheme: Evaluation Over Arctic Field Sites With the ISBA Land Surface Model. *Journal of Advances in Modeling Earth Systems,* 11**:** 293-326. DOI: 10.1029/2018ms001329
Muller, S. W. 1947. Permafrost or permanently frozen ground and related engineering problems. Report, Ann Arbor, MI.
Nash, J. E., J. V. Sutcliffe. 1970. River flow forecasting through conceptual models part I — A discussion of principles. *Journal of Hydrology,* 10**:** 282-290. DOI: 10.1016/0022-1694(70)90255-6
Nelson, F. E., O. A. Anisimov, and N. I. Shiklomanov. 2002. Climate Change and Hazard Zonation in the Circum-Arctic Permafrost Regions. *Natural Hazards,* 26**:** 203-225. DOI: 10.1023/a:1015612918401
Nelson, F. E., N.I. Shiklomanov, G.R. Mueller, K.M. Hinkel, D.A.Walker, and J.G.Bockheim. 1997. Estimating Active-Layer Thickness over a Large Region: Kuparuk River Basin, Alaska, U.S.A. *Arctic and Alpine Research,* 29**:** 367-378. DOI: doi.org/10.1080/00040851.1997.12003258
Nelson, F. E., N. I. Shiklomanov, and G. R. Mueller. 1999. Variability of Active-layer Thickness at Multiple Spatial Scales, North-central Alaska, U.S.A. *Arctic, Antarctic, and Alpine Research,* 31**:** 179-186. DOI: 10.1080/15230430.1999.12003295
NERI. 2000. Documentation for the digital terrain model and orthophoto from Zackenberg. National Environmental Research Institute of Denmark (NERI), Aarhus University (Department of Bioscience). Greenlandic Ecosystem Monitoring (GEM).
Niu, F., J. Luo, Z. Lin, M. Liu, and G. Yin. 2014. Thaw-induced slope failures and susceptibility mapping in permafrost regions of the Qinghai–Tibet Engineering Corridor, China. *Natural Hazards,* 74**:** 1667-1682. DOI: 10.1007/s11069-014-1267-4

Nowinski, N. S., L. Taneva, S. E. Trumbore, and J. M. Welker. 2010. Decomposition of old organic matter as a result of deeper active layers in a snow depth manipulation experiment. *Oecologia*, 163**:** 785-792. DOI: 10.1007/s00442-009-1556-x

O'Neill, P. E., S. Chan, E. G. Njoku, T. Jackson, R. Bindlish, and J. Chaubell. 2020. SMAP Enhanced L3 Radiometer Global Daily 9 km EASE-Grid Soil Moisture, Version 4. Boulder, Colorado USA: National Snow and Ice Data Center Distributed Active Archive Center.

Palmtag, J., S. Cable, H. H. Christiansen, G. Hugelius, and P. Kuhry. 2018. Landform partitioning and estimates of deep storage of soil organic matter in Zackenberg, Greenland. *The Cryosphere*, 12**:** 1735-1744. DOI: 10.5194/tc-12-1735-2018

Permafrost Subcommittee. 1988. Glossary of Permafrost and Related Ground-Ice Terms. In *Technical Memo 142*, Associate Committee on Geotechnical Research. Ottawa: National Research Council of Canada.

Rasmussen, L. H., W. Zhang, J. Hollesen, S. Cable, H. H. Christiansen, P.-E. Jansson, and B. Elberling. 2018. Modelling present and future permafrost thermal regimes in Northeast Greenland. *Cold Regions Science and Technology*, 146**:** 199-213. DOI: 10.1016/j.coldregions.2017.10.011

Reinosch, E., J. Buckel, J. Dong, M. Gerke, J. Baade, and B. Riedel. 2020. InSAR time series analysis of seasonal surface displacement dynamics on the Tibetan Plateau. *Cryosphere*, 14**:** 1633-1650. DOI: 10.5194/tc-14-1633-2020

Rezanezhad, F., J. S. Price, W. L. Quinton, B. Lennartz, T. Milojevic, and P. Van Cappellen. 2016. Structure of peat soils and implications for water storage, flow and solute transport: A review update for geochemists. *Chemical Geology*, 429: 75-84. DOI: 10.1016/j.chemgeo.2016.03.010

Riseborough, D., N. Shiklomanov, B. Etzelmüller, S. Gruber, S. Marchenko. 2008. Recent Advances in Permafrost Modelling. *Permafrost and Periglacial Processes*, 19:2, 137-156. DOI: 10.1002/ppp.615

Sazonova, T. S., and V. E. Romanovsky. 2003. A model for regional-scale estimation of temporal and spatial variability of active layer thickness and mean annual ground temperatures. *Permafrost and Periglacial Processes*, 14**:** 125-139. DOI: 10.1002/ppp.449

Scherler, M., C. Hauck, M. Hoelzle, M. Stähli, and I. Völksch. 2010. Meltwater infiltration into the frozen active layer at an alpine permafrost site. *Permafrost and Periglacial Processes*, 21**:** 325-334. DOI: 10.1002/ppp.694

Schuh, C., A. Frampton, and H. H. Christiansen. 2017. Soil moisture redistribution and its effect on inter-annual active layer temperature and thickness variations in a dry loess terrace in Adventdalen, Svalbard. *The Cryosphere*, 11**:** 635-651. DOI: 10.5194/tc-11-635-2017

Schuur, E. A. G., A. D. McGuire, C. Schädel, G. Grosse, J. W. Harden, D. J. Hayes, G. Hugelius, C. D. Koven, P. Kuhry, D. M. Lawrence, S. M. Natali, D. Olefeldt, V. E. Romanovsky, K. Schaefer, M. R. Turetsky, C. C. Treat and J. E. Vonk. 2015. Climate change and the permafrost carbon feedback. *Nature*, 520**:** 171-179. DOI: 10.1038/nature14338

Seppala, M. 2003. An experimental climate change study of the effect of increasing snow cover on active layer formation of a palsa, Finnish Lapland. *Permafrost, 2***:** 1013-1016.

Short, N., A.-M. Leblanc, W. Sladen, G. Oldenborger, V. Mathon-Dufour, and B. Brisco. 2014. RADARSAT-2 D-InSAR for ground displacement in permafrost terrain, validation from Iqaluit Airport, Baffin Island, Canada. *Remote Sensing of Environment*, 141**:** 40-51. DOI: 10.1016/j.rse.2013.10.016

Skov, K., C. Sigsgaard, M. Rask Mylius, and M. Lund. 2020. GeoBasis Manual Zackenberg. Aarhus University & University of Copenhagen, Report.

Sobiech-Wolf, J., T. Ullmann, and N. Hartmann. 2017. Soil moisture at Zackenberg valley, NE Greenland, July 2014. Alfred Wegener Institute. Bremerhaven: PANGAEA.

Strand, S. M., H. H. Christiansen, M. Johansson, J. Åkerman, and O. Humlum. 2020. Active layer thickening and controls on interannual variability in the Nordic Arctic compared to the circum-Arctic. *Permafrost and Periglacial Processes*. DOI: 10.1002/ppp.2088

Streletskiy, D. A., N. I. Shiklomanov, and F. E. Nelson. 2012. Spatial variability of permafrost active-layer thickness under contemporary and projected climate in Northern Alaska. *Polar Geography*, 35**:** 95-116. DOI: 10.1080/1088937x.2012.680204

Walter, D., and W. Busch. 2012. Influences of DEM quality parameters on the topographic phase correction in DInSAR. *2012 IEEE International Geoscience and Remote Sensing Symposium*, Munich, 3927-3930. DOI: 10.1109/IGARSS.2012.6350553.

Walvoord, M. A., and B. L. Kurylyk. 2016. Hydrologic Impacts of Thawing Permafrost-A Review. *Vadose Zone Journal*, 15**:**6. DOI: 10.2136/vzj2016.01.0010

Walz, J., C. Knoblauch, L. Böhme, and E. M. Pfeiffer. 2017. Regulation of soil organic matter decomposition in permafrost-affected Siberian tundra soils - Impact of oxygen availability, freezing and thawing, temperature, and labile organic matter. *Soil Biology and Biochemistry*, 110**:** 34-43. DOI: 10.1016/j.soilbio.2017.03.001

Wang, C., Z. Zhang, H. Zhang, B. Zhang, Y. Tang, and Q. Wu. 2018. Active Layer Thickness Retrieval of Qinghai–Tibet Permafrost Using the TerraSAR-X InSAR Technique. *IEEE Journal of Selected Topics in Applied Earth Observations and Remote Sensing*, 11**:** 4403-4413. DOI: 10.1109/jstars.2018.2873219

Wang, Q., T. Zhang, H. Jin, B. Cao, X. Peng, K. Wang, L. Li, H. Guo, L. Jia, and C. Lin. 2017. Observational study on the active layer freeze–thaw cycle in the upper reaches of the Heihe River of the north-eastern Qinghai-Tibet Plateau. *Quaternary International*, 440**:** 13-22. DOI: 10.1016/j.quaint.2016.08.027

Wechsler, S. P. 2007. Uncertainties associated with digital elevation models for hydrologic applications: a review. *Hydrology and Earth System Sciences*, 11**:** 1481-1500. DOI: DOI 10.5194/hess-11-1481-2007

Woo, M. 2012. Introduction. In: *Permafrost Hydrology*. 1 – 35. Berlin, Heidelberg: Springer-Verlag

Wright, N., M. Hayashi, and W. L. Quinton. 2009. Spatial and temporal variations in active layer thawing and their implication on runoff generation in peat-covered permafrost terrain. *Water Resources Research*, 45**:** W05414. DOI: 10.1029/2008wr006880

Yu, J. H., L. L. Ge, S. H. Jung, and L. Jeakee. 2007. Accuracy comparison of Differential Interferometric Synthetic Aperture Radar using LiDAR Digital Elevation Model. *IEEE International Geoscience and Remote Sensing Symposium*, Barcelona, 2007, 1970-1973. DOI: 10.1109/Igarss.2007.4423214

Zhang, T. 2005. Influence of the seasonal snow cover on the ground thermal regime: An overview. *Reviews of Geophysics*, 43. DOI: 10.1029/2004rg000157

Zhang, T., R. G. Barry, K. Knowles, J. A. Heginbottom, and J. Brown. 2008. Statistics and characteristics of permafrost and ground-ice distribution in the Northern Hemisphere. *Polar Geography*, 31**:** 47-68. DOI: 10.1080/10889370802175895

Zhang, Y., I. Olthof, R. Fraser, and S. A. Wolfe. 2014. A new approach to mapping permafrost and change incorporating uncertainties in ground conditions and climate projections. *Cryosphere*, 8: 2253-2253. DOI: 10.5194/tc-8-2253-2014

Zhang, X., H. Zhang, C. Wang, Y. Tang, B. Zhang, F. Wu, J. Wang, and Z. Zhang. 2020. Active Layer Thickness Retrieval Over the Qinghai-Tibet Plateau Using Sentinel-1 Multitemporal InSAR Monitored Permafrost Subsidence and Temporal-Spatial Multilayer Soil Moisture Data. *IEEE Access*, 8**:** 84336-84351. DOI: 10.1109/access.2020.2988482

Zhao, L., G. Cheng, S. Li, X. Zhao, and S. Wang. 2000. Thawing and freezing processes of active layer in Wudaoliang region of Tibetan Plateau. *Chinese Science Bulletin*, 45**:** 2181-2187. DOI: 10.1007/bf02886326

8 Appendix

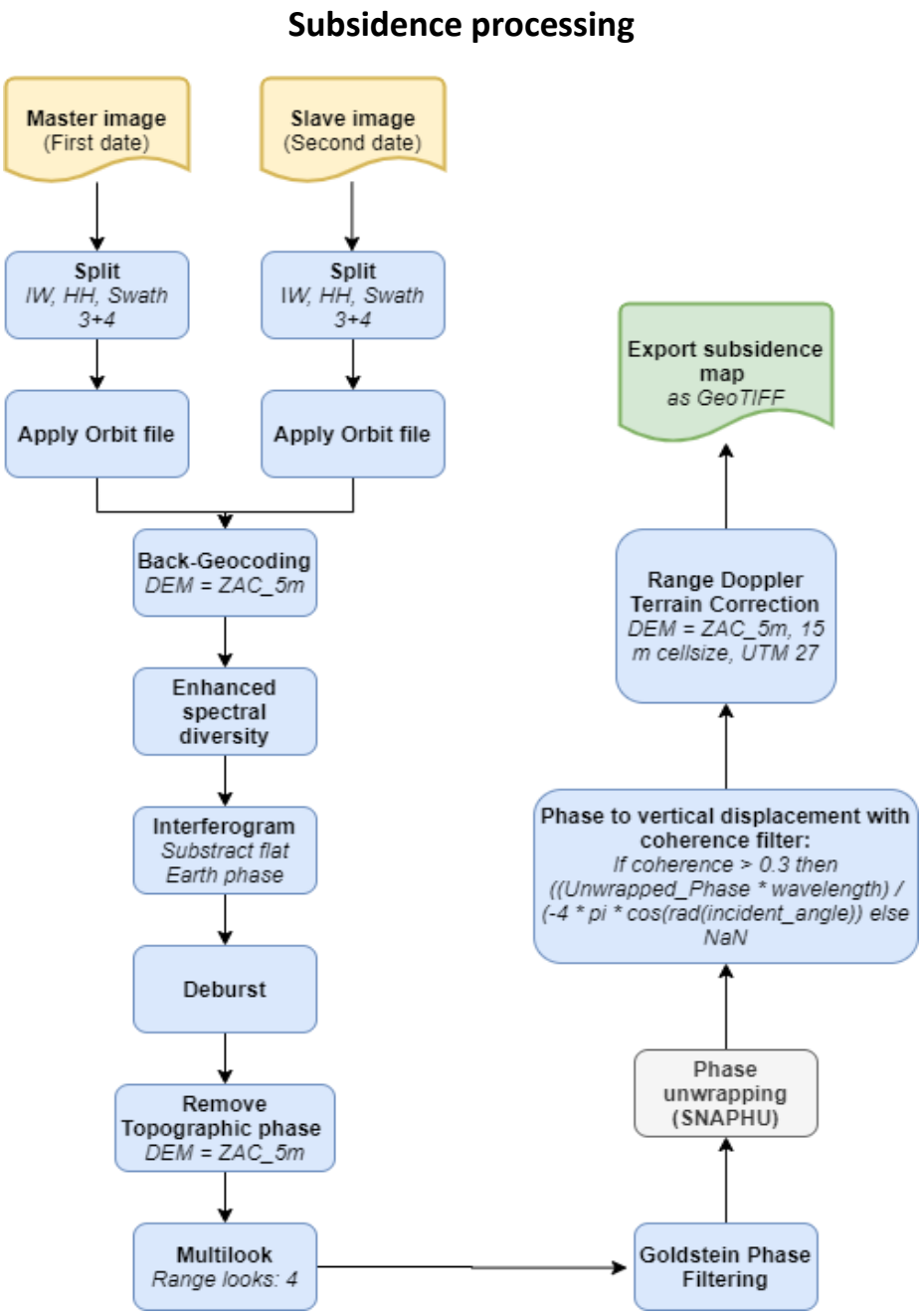

Figure A1: *Flow chart of processing steps in SNAP to derive the subsidence from SAR-imagery.*

Porosity and Saturation fraction calculation

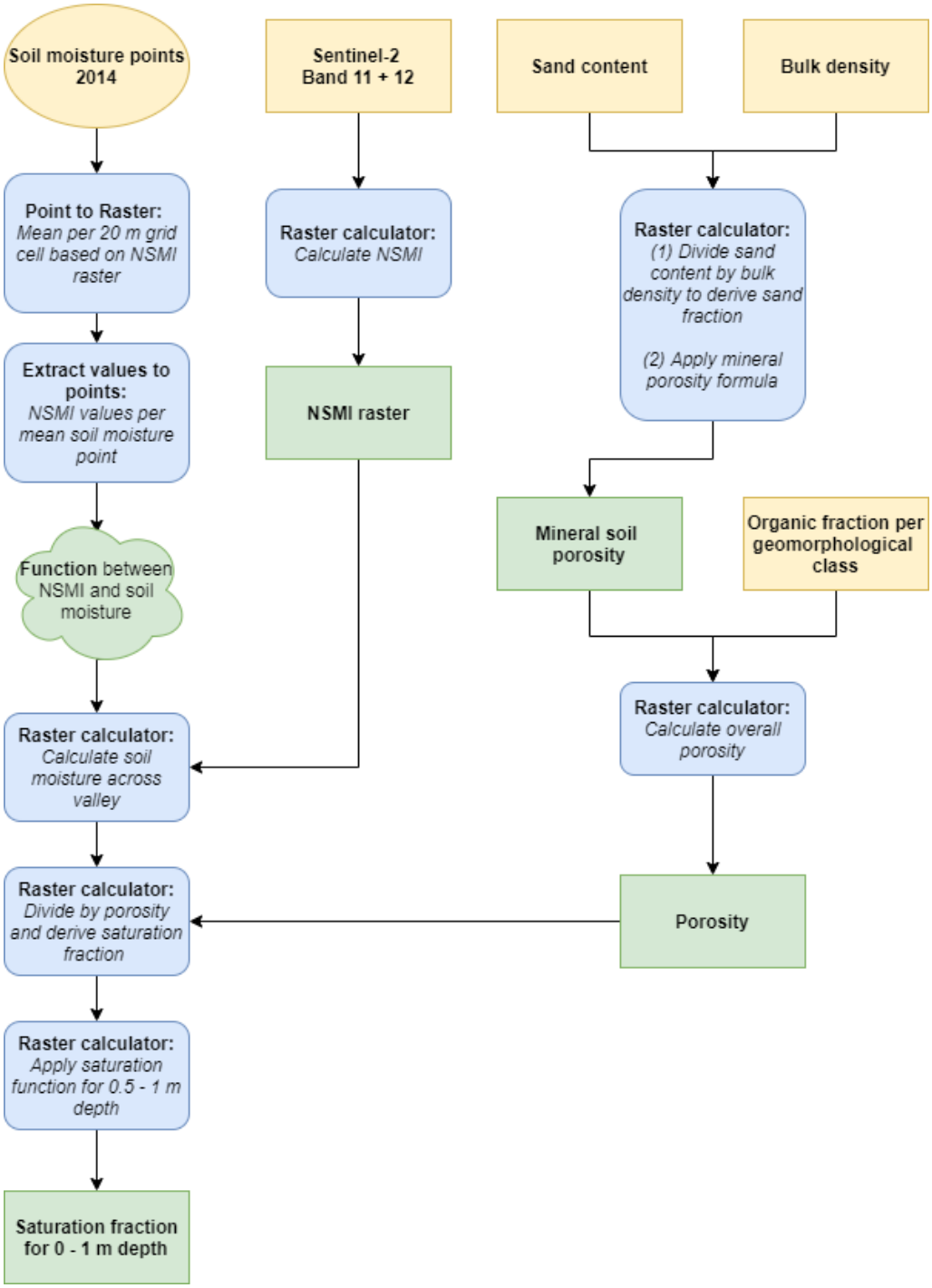

***Figure A2**: Flow chart of processing steps in ArcGIS to estimate the porosity from soil raster data and the saturation fraction from the NDWI-field measurement relationship (Table 1A).*

ALT calculation

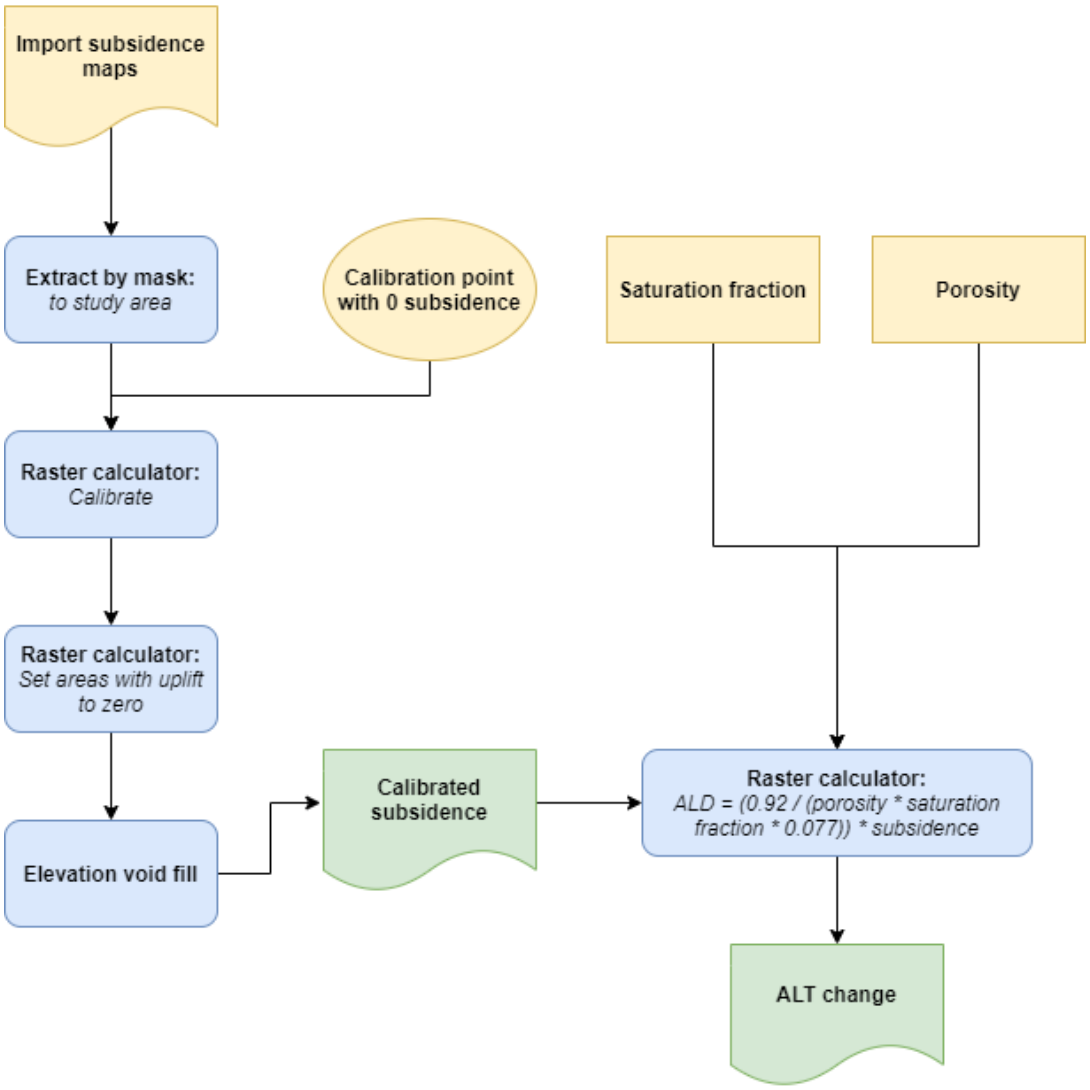

Figure A3*: Flow chart of processing steps in ArcGIS to calculate the ALT from the subsidence, porosity, and saturation fraction estimate.*

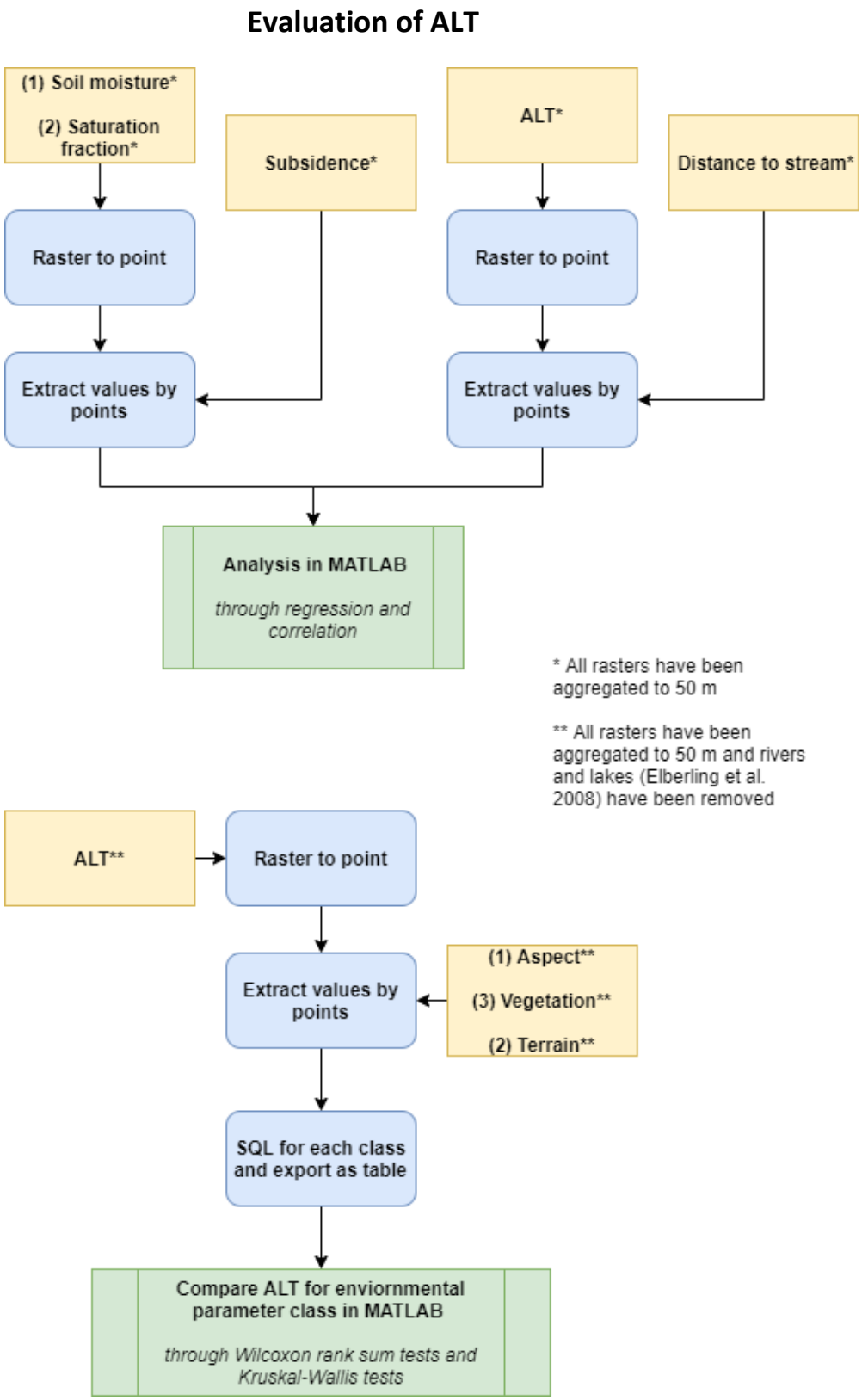

Figure A4: *Flow chart of ALT evaluation in ArcGIS to evaluate the relationship of subsidence to saturation fraction as well as NSMI-based soil moisture, and to evaluate the ALT distribution regarding the environmental factors (stream distance, terrain, aspect, vegetation).*

Table A1: *Overview of used data*

Variable	Description	Source
DEM	2m resolution, aggregated to 5m.	GEM 2000
Satellite image	Sentinel-2 from 12-08-2016 with bands 1 - 12. Bands 2,3,4 used for RGB and bands 11,12 used for NSMI.	ESA 2020b
SAR imagery	Sentinel-1 IW SLC with HH polarization.	ESA 2020b
Vegetation map	12 classes based on remote sensing and field data from 2005.	Elberling et al. 2008
Rivers		GEM 2020b
Temperature-depth measurements	From thermistor strings at Climate Station, Runway, Triangle, Fan and Grassland. For 0 m, 0.25 m, 0.5 m, 0.75 m, 1 m, 1.25 m (except Runway) and 1.5 m soil depth.	GEM 2020a
ALT manual probe measurements	From grids Zerocalm 1 (121 points) and Zerocalm 2 (208 points), MM2 (5 points), AC (8 points).	GEM 2020a
Temperature data	From the Climate station in Zackenberg. Measurements are 60 min average at 2 m height.	GEM 2020a
Precipitation data	Accumulated precipitation over 60 min intervals from Climate station in Zackenberg. Data gaps filled with precipitation data from station MM2.	GEM 2020a
Soil moisture measurements	4538 measurement points taken during 02-07-2017 to 15-07-2014.	Sobiech et al. 2017
Sand weight fraction	250m resolution with estimate for 0.3 – 0.6 m depth.	ISRIC 2020b
Bulk density	250m resolution with estimate for 0.3 – 0.6 m depth.	ISRIC 2020b
Geomorphological classes	Based on Cable et al. 2018 and aggregated into major classes based on Palmtag et al. 2018.	Palmtag et al. 2018
Organic carbon density	For major geomorphological classes over 0-1 m depth.	Palmtag et al. 2018

Table A2: *Processed Sentinel 1-SLC images obtained through ESA (2020b).*

Date	Track	Pass	Satellite	Remarks
12-06-2017	74	Ascending	Sentinel-1A	Excluded due to insufficient coherence
20-06-2017	74	Ascending	Sentinel-1A	
02-07-2017	74	Ascending	Sentinel-1A	
14-07-2017	74	Ascending	Sentinel-1A	
26-07-2017	74	Ascending	Sentinel-1A	
07-08-2017	74	Ascending	Sentinel-1A	
19-08-2017	74	Ascending	Sentinel-1A	
31-08-2017	74	Ascending	Sentinel-1A	

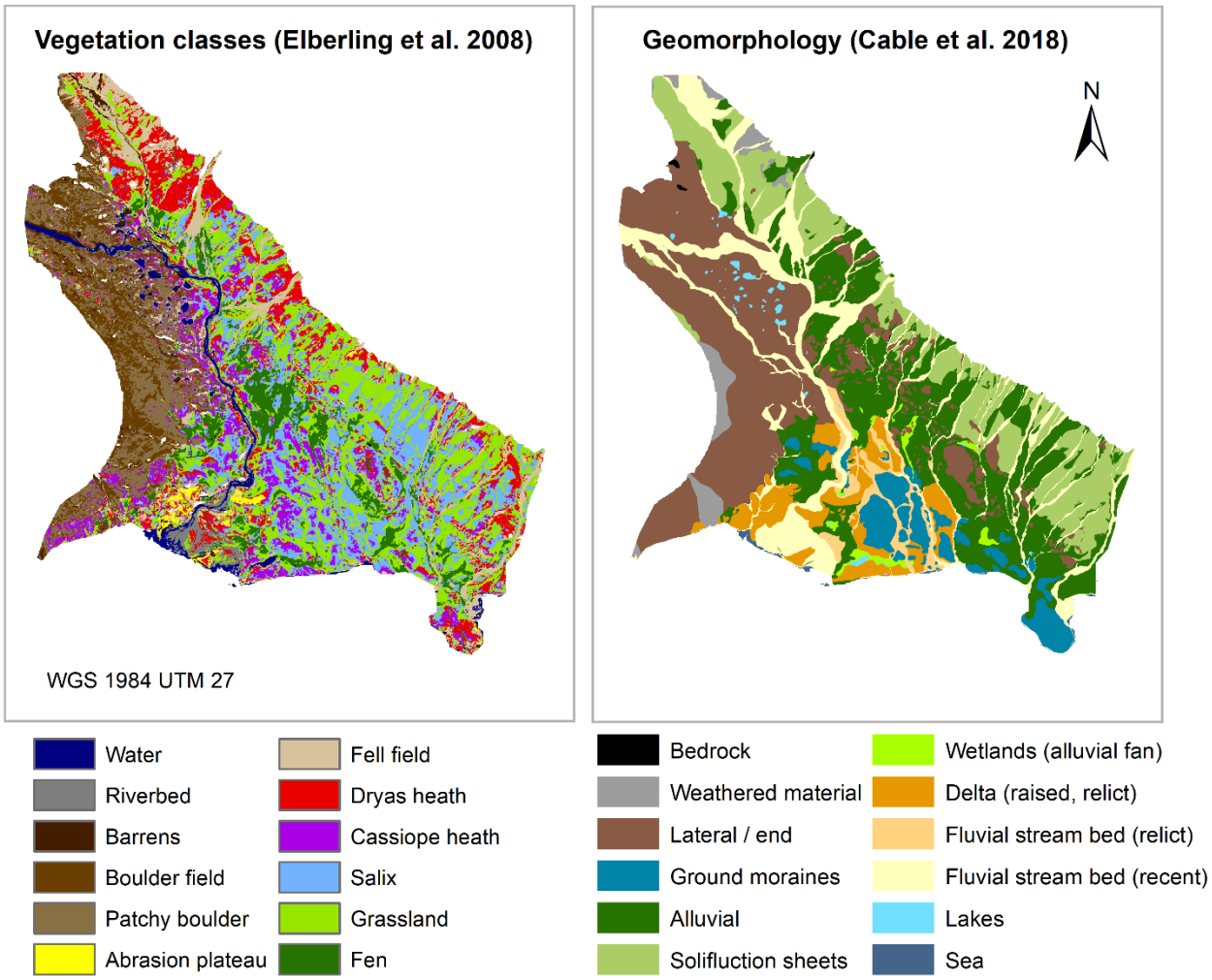

Figure A5: *Vegetation map (left) and map of geomorphological classes (right).*

Table A3: *Classification of vegetation map (Elberling et al. 2008) used for evaluation of estimated ALT.*

Vegetation type analysed	**Vegetation class from Elberling et al. (2008)**
No vegetation	Barrens, Boulder field, Patchy boulder field, Abrasion plateau, Fell field
Vegetation	Dryas heath, Cassiope heath, Salix snow bed, Grassland, Fen
Dryas	Dryas heath
Cassiope	Cassiope heath
Salix	Salix snow bed
Grassland	Grassland
Fen	Fen

Table A4: *Soil organic matter based on carbon density measurements from Palmtag et al. (2018) for adjusted geomorphological classes (Cable et al. 2018).*

Geomorphological class	**Carbon density (kg C/m^2)**	**Soil organic matter fraction (%)**
Weathered material	0.3	0.2
Solifluction sheets	1.7	1.2
Lateral / end moraines	2.1	1.5
Ground moraine	15.9	11.4
Alluvial fans	19.8	14.3
Wetlands (alluvial fan)	29.8	21.3
Fluvial stream bed (relict)	20.9	14.9
Delta (raised, relict)	9.1	6.5
Fluvial stream bed (recent)	1.0	0.7

Table A5: *Linear regression between Grouped soil moisture measurements 2014 and Sentinel-2 band indexes or 5 m resolution DEM (Table A1).*

Index name	Band / DEM combination	R^2	n	Linear function	Reference
Topographical wetness index (TWI)	$\ln \frac{a}{\tan b}$ where a = local upslope area and tan(b) = local slope	0.09	358	soil moisture=1.9164 * TWI + 21.838	Beven and Kirkby 1979
Normalized differential wetness index (NDWI)	$\frac{Band_8 - Band_{12}}{Band_8 + Band_{12}}$	0.41	358	soil moisture=66.421 * NDWI + 27.294	Gao 1996
Normalised soil moisture index (NSMI)	$\frac{Band_{11} - Band_{12}}{Band_{11} + Band_{12}}$	0.64	358	soil moisture=185.83* NSMI - 8.2639	Haubrock et al. 2008

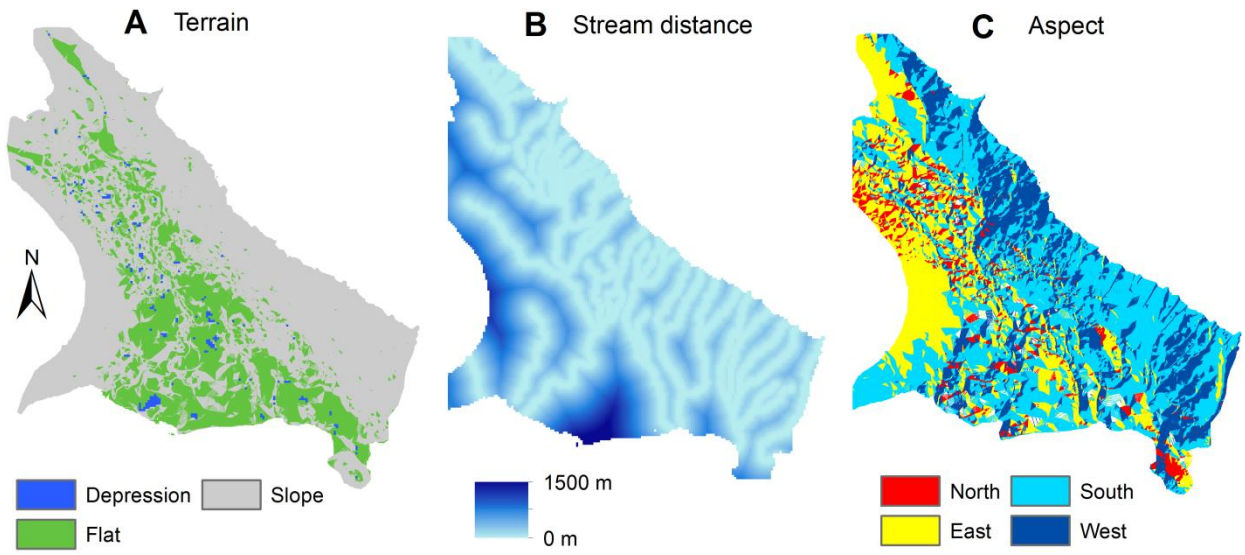

Figure A6: *Environmental parameters. A = Terrain, B = Distance to Stream, C = Aspect*

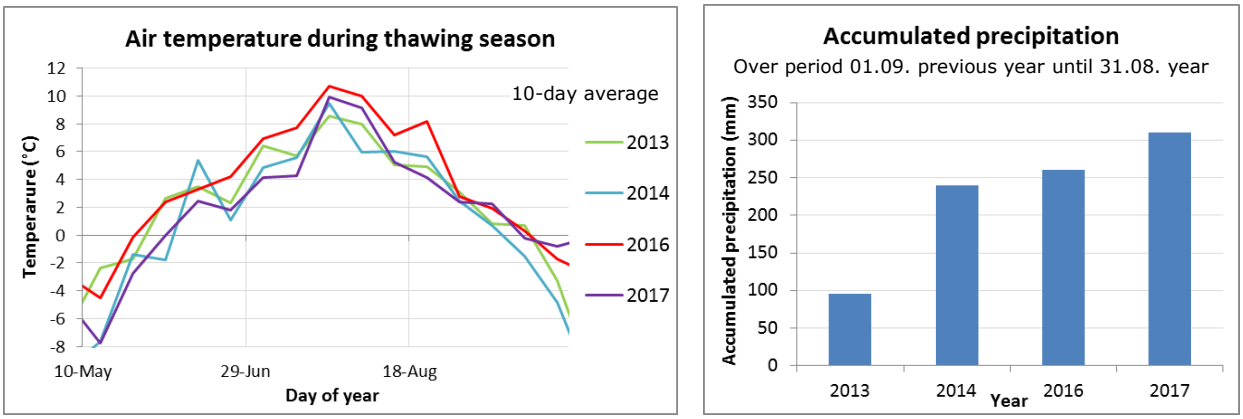

Figure A7: *Temperature and Precipitation for years 2013, 2014, 2016 and 2017 (GEM 2020a). Based on the variables the soil moisture dataset from 2014 (and not the data from 2013) was chosen to estimate the ice content at the end of the thawing season 2016.*

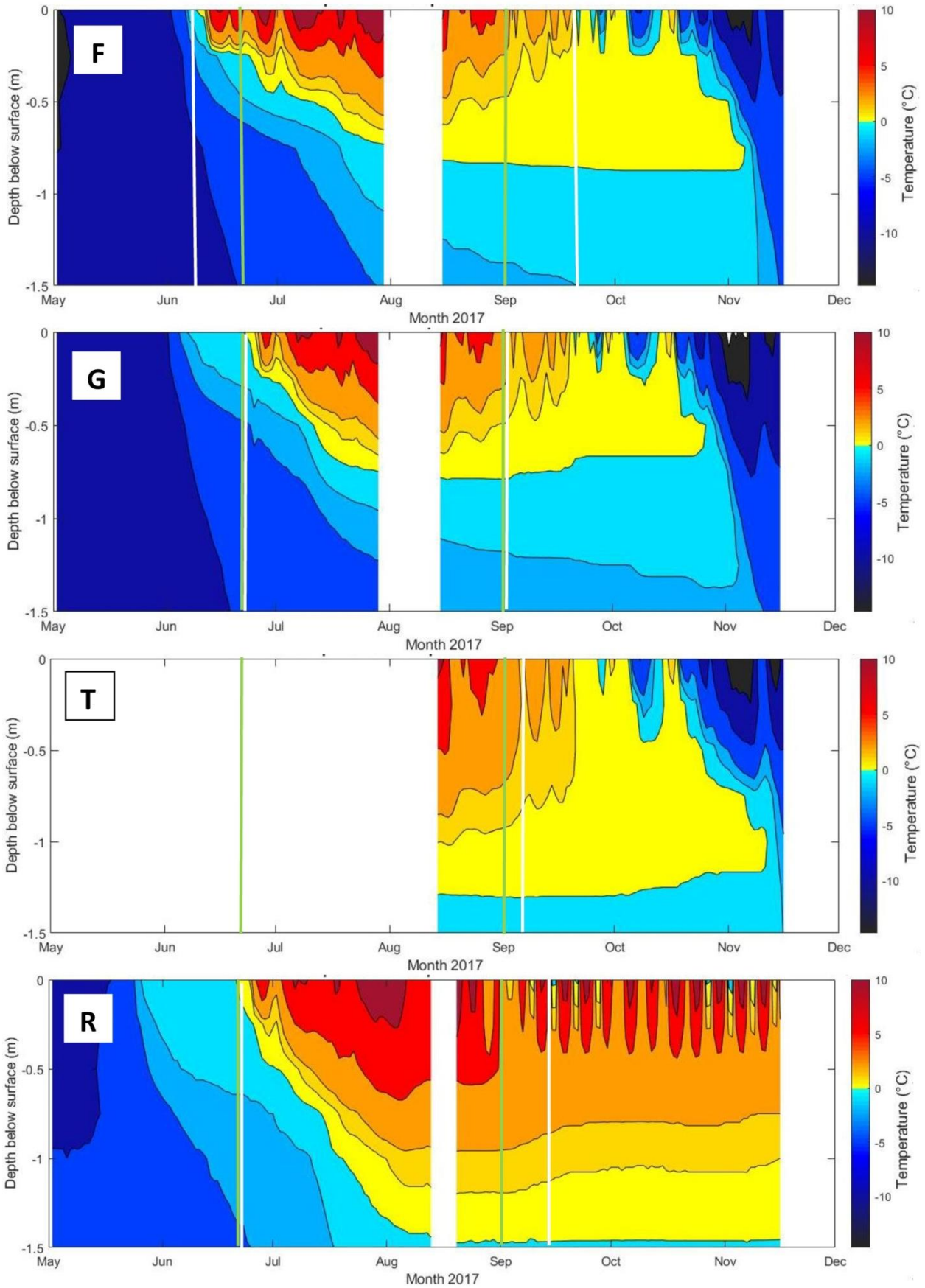

Figure A8: *Soil temperatures at thermistor string sites with red line showing 0 °C isotherm, white lines showing thawing period and green lines DInSAR period.*
F = Fan, G = Grassland, T = Triangle, R = Runway